Ocean Surface Wave Spectra inside Tropical Cyclones

PAUL A. HWANG

Remote Sensing Division, Naval Research Laboratory, Washington, D.C.

YALIN FAN

Oceanography Division, Naval Research Laboratory, Stennis Space Center, Mississippi

FRANCISCO J. OCAMPO-TORRES

Departamento de Oceanografía Física, Centro de Investigación Científica y de Educación Superior de Ensenada, Ensenada, Mexico

HÉCTOR GARCÍA-NAVA

Instituto de Investigaciones Oceanológicas, Universidad Autónoma de Baja California, Ensenada, Mexico

(Manuscript received 3 April 2017, in final form 19 June 2017)

ABSTRACT

Directional wave spectra acquired in hurricane reconnaissance missions are compared with wind-wave spectral models. The comparison result is quantified with two indices of model–measurement spectral agreement. In the main region of hurricane coverage, the indices vary sinusoidally with the azimuth angle referenced to the hurricane heading while showing a weak dependence on the radial distance from the hurricane center. The measured spectra agree well with three models evaluated in the back and right quarters, and they are underdeveloped in the front and left quarters. The local wind and wave directions also show a weak radial dependence and sinusoidal variation along the azimuth. The wind and wave vectors are almost collinear in the back and right quarters; they diverge azimuthally and become almost perpendicular in the left quarter. The azimuthally cyclical correlation between the indices of spectral agreement and the wind-wave directional difference is well described by the sinusoidal variations. Also discussed is the wide range of the spectral slopes observed in both hurricane and nonhurricane field data. It is unlikely that the observed spectral slope variation is caused by Doppler frequency shift from background currents. No clear correlation is found between spectral slope and various wind and wave parameters. The result suggests that the spectral slope needs to be treated as a stochastic random variable. Complementing the existing wind-wave spectral models that prescribe a fixed spectral slope of either −4 or −5, a general spectral model with its spectral parameters accommodating a variable spectral slope is introduced.

1. Introduction

In a small number of hurricane reconnaissance missions, detailed wave measurements inside hurricanes are obtained with an active scanning radar altimeter (Wright et al. 2001; Walsh et al. 2002; Moon et al. 2003; Black et al. 2007; Fan et al. 2009b) and combined with their primary product of the atmospheric measurements; of particular importance to this study is the real-time wind information derived from active and passive microwave and optical sensors as well as other sources through data assimilation (e.g., Powell et al. 1996; Powell and Houston 1998; Dunion and Velden 2002; Dunion et al. 2002).

Together with earlier investigations employing numerical simulations (Young 1988) and ocean buoy recordings (Young 1998, 2006), the hurricane reconnaissance simultaneous and collocated wind and wave data establish the fetch- and duration-limited nature of surface wave growth inside hurricanes (Hwang 2016; Hwang and Walsh 2016; Hwang and Fan 2017) and lead us to tapping the vast wealth of knowledge accumulated from decades of wind-wave research (e.g., Sverdrup and Munk 1947; Pierson

Corresponding author: Paul A. Hwang, paul.hwang@nrl.navy.mil

DOI: 10.1175/JPO-D-17-0066.1

and Moskowitz 1964; Hasselmann et al. 1973; Donelan et al. 1985; Young and van Vledder 1993; Kahma and Calkoen 1992, 1994; Komen et al. 1994; Babanin and Soloviev 1998; Young 1999; Janssen 2004; Hwang and Wang 2004; Zakharov 2005; Badulin et al. 2005, 2007; Hwang 2006a; Gagnaire-Renou et al. 2011; Hwang et al. 2011; Zakharov et al. 2015).

At the foundation of the fetch- or duration-limited wind-wave growth is a couple of equations describing the development of wave height and wave period subject to wind forcing. In other words, for a given fetch or duration, there are two equations connecting the three critical wind and wave parameters (wind-wave triplets): reference surface wind speed U_{10}, significant wave height H_s, and dominant wave period T_p. Consequently, the full set of wind-wave triplets can be derived knowing only one of the three.

Through reverse engineering, Hwang and Fan (2017) present a fetch and duration scaling model of hurricane wind fields derived from simultaneous and collocated wind speed, significant wave height, and dominant wave period collected in four hurricane reconnaissance missions. The fetch and duration scaling model provides the required fetch or duration information for applying the fetch- or duration-limited wind-wave growth functions inside hurricanes.

This development has significant implications on satellite monitoring of tropical cyclones, in particular, to derive wind speed from significant wave height or dominant wave period to bypass the signal saturation problem encountered in microwave radar returns from the ocean surface in high winds (e.g., Hwang 2016; Hwang et al. 2017; Zhang et al. 2017). Furthermore, with regard to air–sea interaction the mechanical energy and momentum exchanges inside hurricanes can be computed because the energy and momentum exchanges of wind seas are functions of the wind-wave triplets (Hwang and Sletten 2008; Hwang and Walsh 2016).

Taking advantage of the wind-sea nature of surface wave development inside tropical cyclones, Hwang and Fan (2017) demonstrate that the spatial distributions of the sea-state parameters and wind-wave energy and momentum exchanges inside the hurricane coverage area as well as their temporal evolution following the hurricane development can be produced using the time series of the 2D wind fields routinely provided by the National Oceanic and Atmospheric Administration (NOAA) Hurricane Research Division (HRD).

The wave data from hurricane reconnaissance missions contain much more than the basic information of significant wave height and dominant wave period. In fact, the scanning radar altimeter (SRA) carried on the hurricane reconnaissance aircraft measures the 3D ocean surface topography to produce the 2D wavenumber spectra along the ground tracks of the aircraft (Walsh et al. 1985, 1989). Here, we present an analysis of the wave spectral properties inside hurricanes with special emphasis on the comparison with several published wind-sea spectral models: Hasselmann et al. (1973, 1976), Donelan et al. (1985), Young (2006), and a spectral model with its spectral parameters accommodating a variable spectral slope (appendix). The precise radial and azimuthal coverage of the hurricane reconnaissance wind and wave datasets provide us the opportunity to explore and quantify the spatial variation of the wave spectra as well as the spectral model performance inside hurricanes.

In the following, section 2 describes the data processing and analysis procedures. Section 3 presents the comparison results and discussion on topics including the azimuthal and radial variations of the indices of agreement between modeled and measured spectra, their dependence on the wind and wave directional difference, the wind and wave propagation directions inside hurricanes, the implications of the hurricane wind and wave observations on wind-wave generation in the presence of background waves or under unsteady wind forcing (in direction or speed), variability of the spectral slope, and the effect on the spectral slope determination from Doppler frequency shift induced by background currents. Section 4 is the summary, and the appendix provides more information on the spectral models used in the comparison analysis to complement the brief description given in section 2b.

2. Hurricane spectral analysis

a. Spectral data processing

For wave measurements, hurricane reconnaissance employs an airborne SRA system to obtain the 3D ocean surface topography (Walsh et al. 1985, 1989). For the data discussed in this paper, the typical cross-flight swath and the sampling spacing on the ocean surface for hurricane wave measurements are 1200 and 25 m, respectively. The nominal wavelength of the shortest resolvable spectral component is 50 m, and the corresponding spectral wavenumber k is 0.13 rad m^{-1}. The archived SRA 2D wavenumber spectra $S(k_1, k_2)$ are stored as 65 by 65 matrices with spectral resolution $dk = 0.0035$ rad m^{-1}, k_1 and k_2 are, respectively, the east and north components of the wavenumber vector, and their maxima in the archived data are 0.11 rad m^{-1} with the corresponding intrinsic angular frequency of 1.04 rad s^{-1}. Altogether, four datasets collected in deep

TABLE 1. Basic information of the four datasets used for the analysis in this paper; they were collected in hurricane Bonnie 1998 (B24) and Ivan 2004 (I09, I12, and I14); copied from Table 1 of Hwang and Fan (2017).

Data ID	B24	I09	I12	I14
Start time	2029 UTC 24 Aug 1998	1615 UTC 9 Sep 2004	1039 UTC 12 Sep 2004	2009 UTC 14 Sep 2004
End time	0144 UTC 25 Aug 1998	2010 UTC 9 Sep 2004	1541 UTC 12 Sep 2004	0249 UTC 15 Sep 2004
HRD U_{10} max (m s^{-1})	44.4	59.4	55.4	61.6
HRD r_m (km)	74.0	13.0	17.0	42.0
HRD ϕ_m (°)	307.0	240.0	255.0	240.0
V_h (m s^{-1})	4.5	5.6	4.3	4.8
ϕ_h (degN)	13.0	62.0	66.0	25.0
SRA U_{10} min (m s^{-1})	1.4	1.8	0.8	1.2
SRA U_{10} max (m s^{-1})	45.7	74.0	59.9	69.6
SRA H_s min (m)	4.4	1.6	2.9	3.6
SRA H_s max (m)	10.9	12.7	12.0	13.1
SRA T_p min (s)	8.0	5.8	8.2	8.9
SRA T_p max (s)	13.3	15.2	13.8	14.4
Number of SRA spectra	233	376	456	600

water and unaffected by bathymetry are available for analysis (Table 1). More detailed information about the four datasets has been reported in earlier publications (Wright et al. 2001; Walsh et al. 2002; Moon et al. 2003; Fan et al. 2009b; Hwang and Fan 2017).

For comparison with spectral models, the 2D wavenumber spectrum $F(k_1, k_2)$ is integrated azimuthally to yield the 1D wavenumber spectrum $S(k)$ and then converted to the 1D frequency spectrum $S(\omega)$ through

$$F(k_1, k_2)\, dk_1\, dk_2 = F(k, \theta)\, k\, dk\, d\theta = S(k, \theta)\, dk\, d\theta, \qquad (1)$$

and

$$S(\omega)\, d\omega = S(k)\, dk = \int_{-\pi}^{\pi} S(k, \theta)\, dk\, d\theta. \qquad (2)$$

The frequency spectra are then interpolated to the angular frequency range between 0.2 and 1.0 rad s^{-1} with uniform spacing of 0.01 rad s^{-1}. Figure 1 shows an example of the resulting frequency spectra in eight sectors of the hurricane coverage area (two sectors for each quarter; see inset). The highest spectral peak frequency ω_p is observed in the back sector B1. The ω_p magnitude decreases systematically counterclockwise (CCW), reaching its lowest value near the front, and then slowly increases toward the back. Within the same sector, the variation of spectra with respect to range from the hurricane center is relatively small compared to the azimuthal variation. These results are consistent with the radial and azimuthal variations of the integral wave properties (significant wave height and spectral peak wave period) discussed in previous publications (Hwang 2016; Hwang and Walsh 2016; Hwang and Fan 2017). For example, Fig. 13 in Hwang and Fan (2017) illustrates the azimuthal variations of U_{10}, H_s, and T_p at several radial distances from the hurricane center for the four datasets.

b. A brief discussion of spectral models

Most published spectral models of deep-water, wind-generated surface waves prescribe a constant spectral slope of either −4 or −5 in the high-frequency region. For example, the most influential wind-wave spectral model is attributed to Pierson and Moskowitz (1964) describing the fully developed seas in the open ocean and is referred to as the P model in this paper. The P model is given as a power-law function in the high-frequency portion and an exponential function to give the bell-shaped spectral energy distribution near the peak region. These key features are adopted in subsequent wind-sea spectral models. The spectral slope in the high-frequency region is −5 for the P model, mainly based on the dimensional analysis and similarity consideration of the short-scale waves in the saturation or equilibrium range (Phillips 1958a,b; Kitaigorodskii 1961).

Hasselmann et al. (1973, 1976) present results from a large-scale, fetch-limited, wind-generated wave measurement program [Joint North Sea Wave Project (JONSWAP)] consisting of 13 wave stations along a 160-km profile extending westward from the west coast of Island of Sylt, Germany, into the North Sea. They introduce a spectral function fashioned after the P model and multiplied with a peak enhancement factor to describe the observed variations in the width and amplitude of the spectral peak. The spectral slope in the high-frequency region remains −5. This model is referred to as the J model in this paper.

Donelan et al. (1985) perform frequency–wavenumber spectral analysis of wave records obtained by a 14-element wave gauge array in Lake Ontario, Canada. The high-frequency spectral slope for the proposed

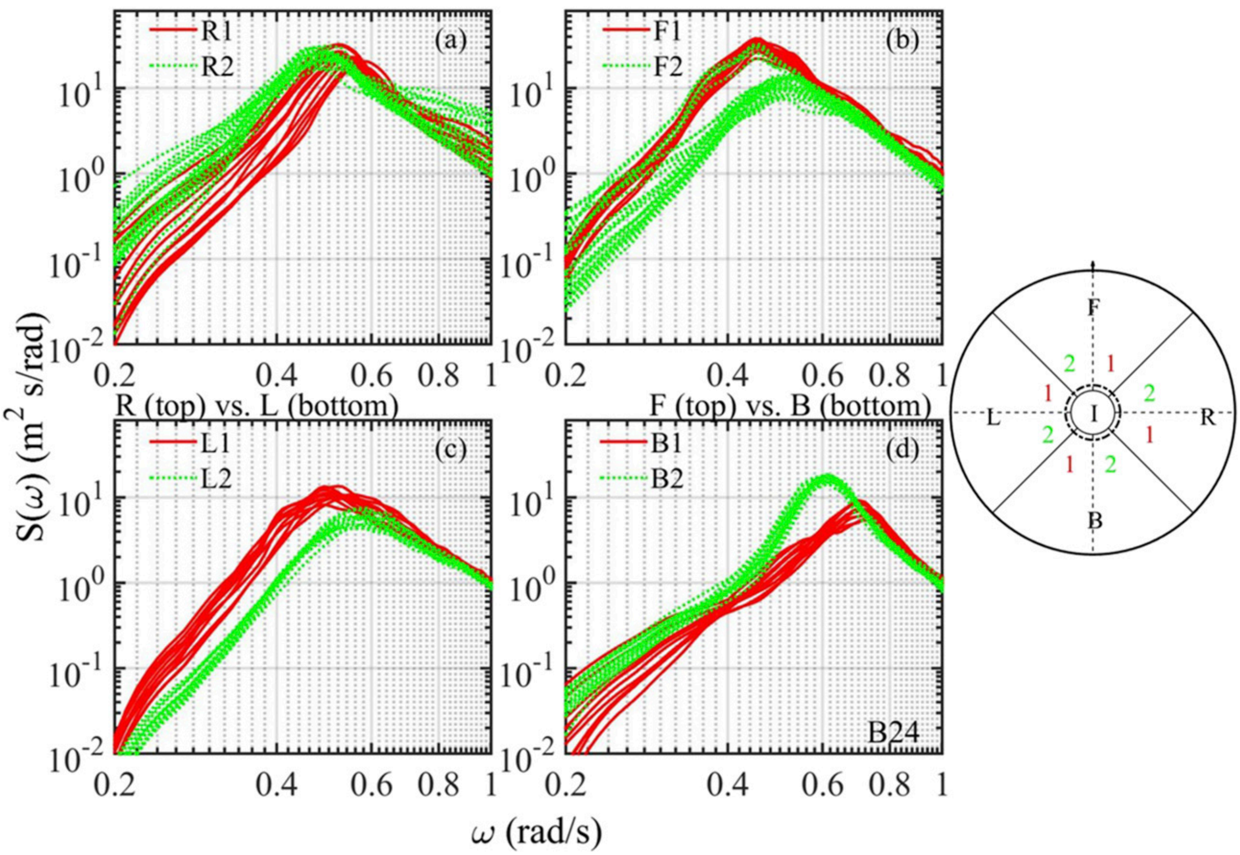

FIG. 1. An example of the wave spectra acquired in hurricane reconnaissance missions; dataset B24 is illustrated. The spectra are sorted into eight sectors (two for each quarter as shown in the inset): (a) R1 and R2, (b) F1 and F2, (c) L1 and L2, and (d) B1 and B2.

model is -4, which many contemporary researchers have advocated; see the review in their section 5.2 or Phillips (1985). The peak enhancement factor and the exponential function for the bell-shaped spectral energy distribution near the spectral peak remain similar to the J and P models, respectively. The Donelan et al. (1985) spectral function is referred to as the D model in this paper.

The measured spectral slope $-s$ in the high-frequency region varies over some range. For example, Young (1998) shows a scatterplot of spectral slopes from his analysis of hurricane-generated directional wave spectra collected over a 16-yr period off the northwest coast of Australia. Many of the spectral slopes fall between -3 and -6; the mean value is -4.56. Young (2006) presents a spectral function taking into account the spectral slope variability, but the impact of the spectral slope does not extend to the associated spectral coefficients. The Young (2006) spectral function is referred to as the Y model in this paper.

The wide range of the spectral slopes as determined by the spectral components in the neighborhood of the spectral peak: $1.5\,\omega_p$ to $3\,\omega_p$ (Donelan et al. 1985) or $2\,\omega_p$ to $4\,\omega_p$ (Young 1998, 2006) is unlikely caused by the Doppler frequency shift induced by the background currents, including the mean current, surface wind drift, and orbital velocity of long waves (section 3f). In the appendix, we introduce a general surface wave spectral model with the associated spectral coefficients incorporating the variable spectral slope (the G model). The mathematical expressions of the P, J, D, Y, and G models are given in the appendix.

c. *Method of comparing spectral models with measurements*

Figure 2 shows four examples of comparing measured and modeled wave spectra (two each for the left and right half planes). To highlight the differences in the neighborhood of the spectral peak, they are also presented in linear scales in Fig. 3. The corresponding 2D wavenumber spectra are shown in section 3d (Fig. 12) and will be further discussed there. These wave spectra are from hurricane Bonnie 1998, for which Wright et al. (2001) have given very comprehensive discussion complemented with 60 representative 2D spectra at various locations insider the hurricane.

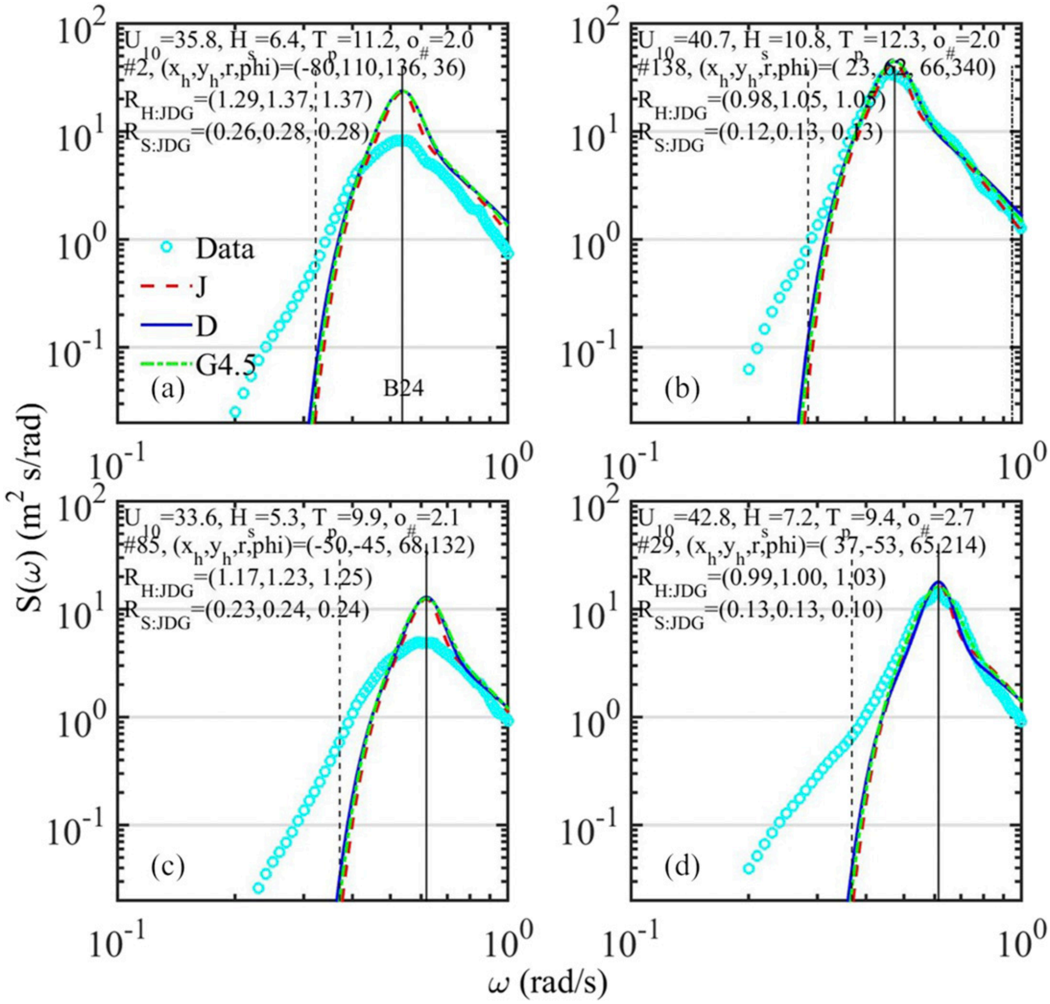

FIG. 2. An example showing the comparison of measured spectra inside hurricanes with three wind-wave spectral models (J, D, and G). Illustrated are results in four different sectors (see inset in Fig. 1): (a) F2, (b) F1, (c) L2, and (d) B2. Four lines of text are printed in each figure. Line 1: (U_{10}, H_s, T_p, $\omega_\#$). Line 2: spectrum sequence number, the position vector (x_h, y_h), and (r, ϕ) rotated with reference to the hurricane heading. Line 3: height index R_H for the J, D and G models. Line 3: spectral index R_S for the J, D, and G models.

To quantify the differences between the measured and modeled wave spectra, as shown in Figs. 2 and 3, we compute two quantities. The first is the integrated spectral variance $\eta_{\rm rms}^2$ or equivalently the significant wave height H_s:

$$\eta_{\rm rms}^2 = \int S(\omega)\,d\omega; \quad H_s = 4\eta_{\rm rms}. \tag{3}$$

The second quantity measures the component-by-component rms difference between model and measurement:

$$\sigma_S = \int \left\{[S_{\rm model}(\omega) - S_{\rm SRA}(\omega)]^2\right\}^{0.5} d\omega, \tag{4}$$

where the subscript model can be J, D, Y, or G, and subscript SRA represents the measured spectrum. The dimensionless ratios $R_H = H_{sm}/H_s$ and $R_S = \sigma_S^{0.5}/H_s$ are referred to as the height and spectral indices, respectively, in subsequent discussions; H_{sm} is the modeled H_s.

Because the observed spectral peak frequency of the hurricane wave data is typically between about 0.4 and 0.7 rad s^{-1} and the upper bound of the measured spectral frequency is 1 rad s^{-1}, the spectral slope cannot be reliably obtained from the hurricane reconnaissance measurements. The significant wave height is slightly impacted by the missing high-frequency components: about 5% to 10% short assuming a high-frequency tail of −4.5 slope. The comparison with spectral models is

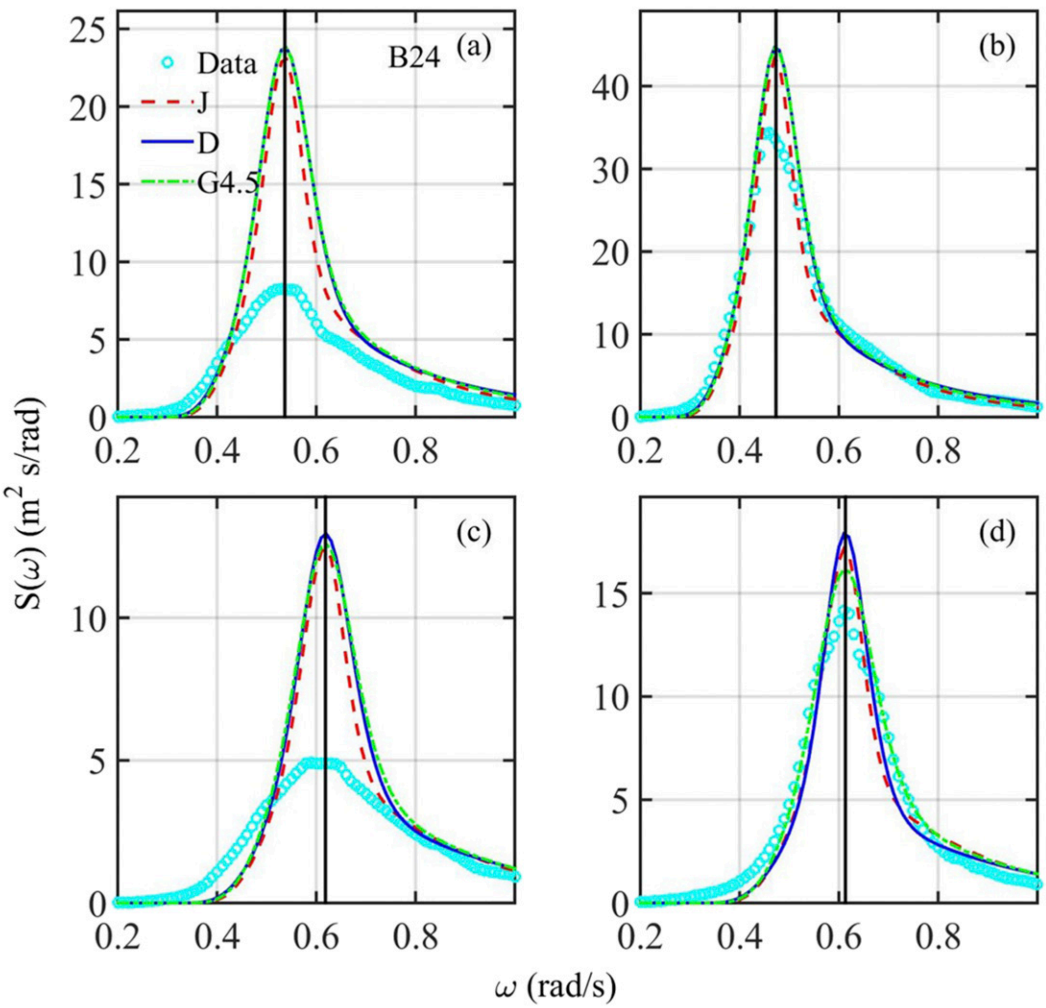

FIG. 3. As in Fig. 2, but presented in linear scales to highlight the differences near the spectral peak region.

limited to the measured spectral components, that is, models use the same frequency range and resolution of the measured spectrum (0.2 to 1 rad s^{-1} in steps of 0.01 rad s^{-1}). The measured peak wave frequency and wind speed are used for computing all spectral models so the model–measurement comparison is on equal footing but limited to a range generally less than 1.6 ω_p to 2.5 ω_p; the missing high-frequency region is not critical to the calculation of wave height or wave energy because of the small magnitude there.

Making use of Young's (1998) hurricane wave spectral slope data described earlier, the G spectrum is computed with $s = 4.5$. The results of the Y spectral model are not shown because they are the same as the D or J model, depending on the choice of the D or J spectral coefficients; see further discussion in the appendix.

Despite the limited frequency range in the hurricane reconnaissance wave spectral data, they represent very precious measurements for examining spectral models in high-wind applications. Qualitatively, the agreement between measured and modeled wave spectra is generally better in the back and right region (ϕ between about 135° and 360°) than that in the front and left region (ϕ between about 0° and 135°). This is consistent in general with previous analyses of the integral wind and wave properties (U_{10}, H_s, and T_p). For example, the analysis of the wind-wave growth in terms of the wave age similarity $\eta_\#(\omega_\#)$ shows that the back and right quarters are generally in very good agreement with the reference curves of $\eta_\#(\omega_\#)$ obtained in steady wind forcing conditions (e.g., Hasselmann et al. 1973; Donelan et al. 1985; Hwang and Wang 2004), and subpar growth is found in the left-quarter data (see Fig. 2 of Hwang and Fan 2017). The dimensionless parameters in the wave age similarity function are $\eta_\# = \eta_{\mathrm{rms}}^2 g^2 U_{10}^{-4}$ and $\omega_\# = \omega_p U_{10} g^{-1}$, where the rms wave elevation η_{rms} is

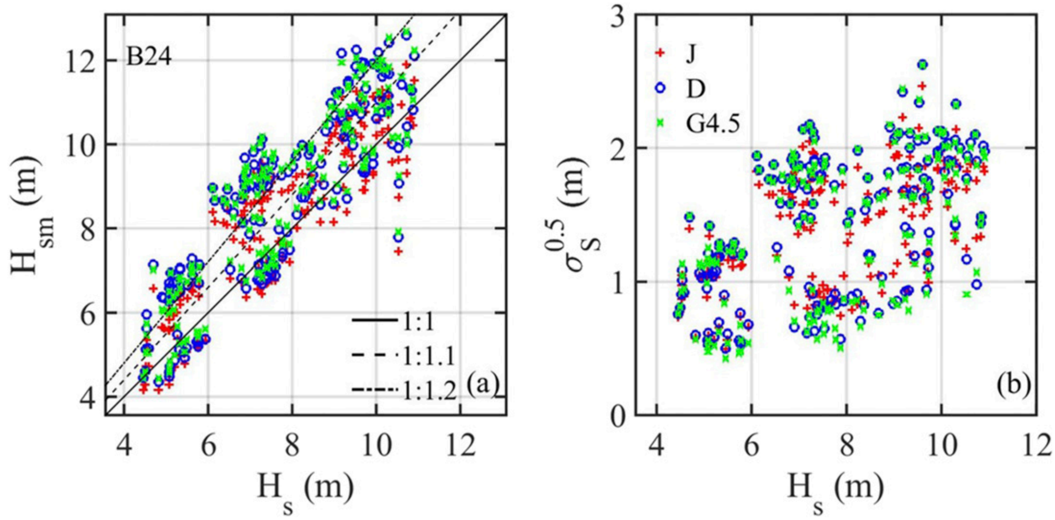

FIG. 4. (a) Comparison of modeled significant wave height H_{sm} with the measured value H_s. (b) Comparison of the integrated component-by-component difference of the modeled $\sigma_S^{0.5}$ vs H_s. Results for J, D, and G (with $s = 4.5$) models are illustrated. For reference, line segments with slopes 1:1, 1:1.1, and 1:1.2 are added in (a).

related to the significant wave height by $H_s = 4\eta_{\mathrm{rms}}$, and the angular frequency of the spectral peak component ω_p is $2\pi T_p^{-1}$. Also, waves in the back and right quarters are younger wind seas, whereas those in the front and left quarters tend to be older wind seas. The dimensionless frequency (inverse wave age) is from about 2 to 4 in the back and right quarters and from about 1 to 3 in the front and left quarters (see Fig. 14 of Hwang and Fan 2017).

Making use of the precise radial and azimuthal information of the hurricane reconnaissance datasets, the model–measurement spectral comparison is processed to yield quantitative results, which are presented in the next section.

3. Results and discussion

a. Overall comparison

An example of comparing the measured and modeled spectra is shown in Fig. 4, the dataset used for this illustration is B24 (Bonnie 1998; Table 1). The significant wave height is given in Fig. 4a; H_{sm} denotes the modeled, where subscript m can be J, D, or G when distinction is needed, and H_s denotes the measured. The integrated component-by-component difference is given in Fig. 4b, shown with $\sigma_S^{0.5}$ for dimensional consistency with the reference variable H_s. Results from three models are displayed with different markers (red +, blue o, and green x, respectively, for J, D, and G with $s = 4.5$). The results from the other three datasets (Table 1) are very similar. The statistics of bias b_0, slope of linear regression b_1, rms difference b_2, and correlation coefficient b_3 for the four datasets are listed in Table 2.

On average, the measured wave height inside a hurricane is lower than the wind-sea spectral model prediction by about 10% to 20%, as estimated from b_1 of the four datasets (Table 2). Because the data quality of dataset I09 appears to be somewhat worse than the others, as deduced from the more zigzagged flight tracks, see discussion in Hwang and Fan (2017), we place less weight on the statistics of I09. There are, however, considerable spatial variations, which are discussed next in section 3b. Based on the numbers listed in Table 2, the J model performs slightly better for the H_s prediction, followed by the G model and then the D model. The component-by-component spectral difference $\sigma_S^{0.5}$ is very similar among the three models (Fig. 4b; Table 2).

Although, as mentioned in section 2b, the frequency resolution of the hurricane wave data are limited to less than about $1.6\omega_p$ to $2.5\omega_p$, these results suggest that various proposed spectral models produce comparable integral wave property in terms of the significant wave height or total wave variance, and they yield almost equally good agreement with field data. Similarly, the conclusions on the radial and azimuthal variations to be discussed in section 3b are not impacted by the shortcoming of the limited frequency resolution in the hurricane wave data. To illustrate the points, the Gulf of Tehuantepec Air–Sea Interaction Experiment (INTOA; García-Nava et al. 2009; Ocampo-Torres et al. 2011; Hwang et al. 2011) measurements are compared with the spectral models, and the statistics of H_{sm} and $\sigma_S^{0.5}$ are also listed in Table 2. The INTOA sampling

TABLE 2. Statistics of bias, slope of linear regression, rms difference, and correlation coefficient (b_0, b_1, b_2, and b_3, respectively) of comparing the modeled and measured spectra, processed in terms of the (a) significant wave height H_{sm} vs H_s and (b) component-by-component spectral difference $\sigma_S^{0.5}$ vs H_s. Four datasets (B24, I09, I12, and I14) and three spectral models (J, D, and G with $s = 4.5$) are used in this study.

	b_0 (m)	b_1	b_2 (m)	b_3
(a) Significant wave height				
B24				
J	−0.007	1.064	1.049	0.883
D	−0.015	1.124	1.429	0.859
G	−0.012	1.131	1.419	0.879
I09				
J	−0.115	1.249	2.007	0.765
D	−0.176	1.380	2.718	0.725
G	−0.139	1.341	2.460	0.758
I12				
J	−0.049	1.126	1.537	0.723
D	−0.078	1.200	2.024	0.651
G	−0.062	1.199	1.921	0.706
I14				
J	−0.023	1.125	1.624	0.778
D	−0.054	1.220	2.346	0.704
G	−0.032	1.201	2.111	0.764
INTOA				
J	0.012	0.832	0.259	0.928
D	0.017	0.882	0.223	0.916
G	0.014	0.886	0.213	0.925
Gs	0.015	0.883	0.214	0.927
(b) Spectral difference				
B24	b_0 (m)	b_1	b_2 (m)	b_3
J	0.016	0.173	6.612	0.540
D	0.012	0.182	6.546	0.512
G	0.013	0.179	6.569	0.479
I09				
J	0.013	0.216	4.708	0.436
D	0.012	0.226	4.658	0.424
G	0.014	0.231	4.639	0.406
I12				
J	0.013	0.185	5.751	0.361
D	0.013	0.198	5.666	0.367
G	0.015	0.194	5.693	0.315
I14				
J	0.026	0.197	6.567	0.439
D	0.027	0.207	6.496	0.401
G	0.031	0.207	6.502	0.345
INTOA				
J	−0.003	0.303	0.884	0.963
D	−0.002	0.300	0.887	0.959
G	−0.002	0.300	0.887	0.959
Gs	−0.002	0.301	0.887	0.959

frequency is 20 Hz, and the spectral slope is determined by the frequency band between $2\,\omega_p$ and $4\,\omega_p$, following the procedure of Young (1998, 2006). Two sets of G spectral model computations are obtained to compare with measurements. The first set uses the constant $s = 4.5$, as done for the hurricane wave comparison. The second set uses the actually measured spectral slope for each spectrum. The statistical results are shown in Table 2 under the labels G and Gs, respectively, for the G model.

From the tabulated numbers, the statistics of the three models are more mixed for the INTOA data. The G spectral model performs well in terms of b_1 and b_2; the J model is slightly better in b_0 and b_3. Furthermore, the G model using the actually measured slope does not produce better results than assuming constant $s = 4.5$.

It is also interesting to notice that for the INTOA data, the spectral models underpredict the measured wave height by about 11%–12% (G and D models) to 17% (J model) based on the b_1 values in Table 2a. The INTOA experiment is conducted in a location with constant presence of counterswell and during several mountain gap wind episodes with wind speeds rapidly increasing or decreasing. The spectral comparison result presented here is consistent with the observation described in Hwang et al. (2011) that the wave generation process becomes more efficient in the presence of background oscillation in a similar sense that a machine runs more efficiently after warming up. For the INTOA experiment, the wind velocity and the resulting wind sea are in the same direction. For the hurricane wind field, the wind and wave angles may differ considerably and further complicate the wind-wave generation process. The issue is deferred to section 3e after the discussion of wind and wave propagations inside hurricanes (sections 3c and 3d).

Although the impact of the high-frequency portion of the wave spectrum to the total wave variance or significant wave height is insignificant, the pursuit of an accurate determination of the spectral slopes for the spectral components beyond the spectral peak region, however, is important to the understanding of the wave dynamics in the equilibrium spectral range that has significant implications in many ocean surface processes such as wave breaking, whitecaps, and surface roughness (e.g., Phillips 1985). Although these subjects are out of the scope of the present study, it is worth noting that the present foundation of the spectral and statistical properties of the equilibrium range in wind-generated gravity waves, as detailed in Phillips (1985), is built upon an $s = 4$ frequency spectral function. Varying the s value can produce orders of magnitude differences in the short-wave properties such as the mean-square slopes [see, e.g., discussion in sections 3 and 5 of Hwang and Wang (2001) and Fig. 10 of Hwang et al. (2013)].

b. Azimuthal and range variations

The azimuthal and range variations of the model–measurement spectral comparison are presented with the dimensionless ratios R_H and R_S, which are the height and spectral indices, respectively (section 2c). For

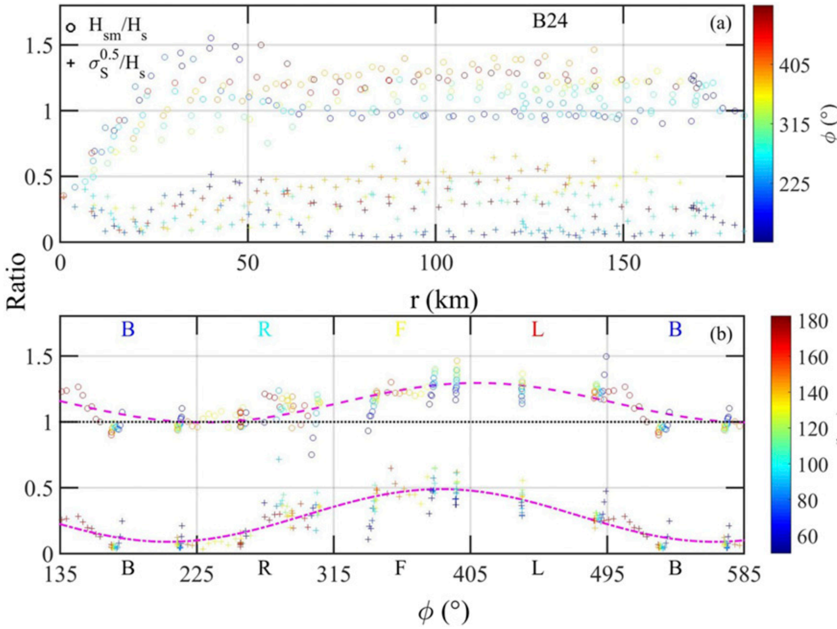

FIG. 5. (a) Radial and (b) azimuthal variations of R_H and R_S; the color coding is ϕ for the former and r for the latter. Sinusoidal curves fitting through the data are shown in (b); the fitted coefficients are listed in Table 3.

perfect agreement between model and measurement, $R_H = 1$ and $R_S = 0$; an example is given in Fig. 5 showing the B24 dataset. The result from the G model is used for this illustration; the J and D models produce similar outcome of comparison. Figure 5a depicts the R_H and R_S dependence on range; the azimuth angle color coding is arranged such that the number on the color map increases in the order of back, right, front, and left quarters, that is, the ϕ range for the plotting is from 135° to 495°. This sequence corresponds approximately to the order of increasing wave age (Hwang 2016; Hwang and Walsh 2016; Hwang and Fan 2017). The azimuth angle ϕ is referenced to the hurricane heading and increases CCW.

The most distinct feature of the spatial pattern is the sinusoidal azimuthal variation revealed in Fig. 5b, showing data with r between 50 and 200 km to minimize swell contamination (Hwang 2016; Hwang and Walsh 2016; Hwang and Fan 2017). In comparison, the trend of radial variation is very mild along transects of constant azimuth angles, except for the region near the hurricane center (Fig. 5a).

Both R_H and R_S can be fitted by a sinusoidal function:

$$R_q = a_{0q} + a_{1q}\cos(\phi + \delta_q), \tag{5}$$

where subscript q is H or S. The coefficients a_0 and a_1 and the lag δ (in degrees) are listed in Table 3 for the four datasets. Based on the fitted curves, the azimuthal locations where R_H is closest to 1 and R_S is closest to 0 are also listed in Table 3 as ϕ_{min}. They vary from 211° to 241° for R_H and from 200° to 222° for R_S in the four datasets. The R_H and R_S values at ϕ_{min} are listed in the fifth column of the table.

c. Wind and wave directions

The hurricane reconnaissance wind and wave data provide detailed information on the wind vector and directional wave spectrum at each measurement location. Figure 6 shows the wind and wave directions ϕ_U and ϕ_w, respectively, processed from the four datasets; ϕ_U and ϕ_w are referenced to the normal **n** of the local position vector (x, y), as indicated in the inset. For waves, we only process

TABLE 3. Coefficients of fitted sinusoidal azimuthal variations of R_H and R_S. The results are based on the G model for the four datasets (B24, I09, I12, and I14).

	a_0	a_1	δ	ϕ_{min}	$R_{H\min}-1$
R_H					
B24	1.15	−0.15	129.70	230.30	0.00
I09	1.40	−0.38	127.12	232.88	0.02
I12	1.35	−0.32	148.52	211.48	0.03
I14	1.19	−0.17	119.05	240.95	0.02
	a_0	a_1	δ	ϕ_{min}	$R_{S\min}$
R_S					
B24	0.29	−0.20	154.15	205.85	0.09
I09	0.40	−0.36	148.44	211.56	0.04
I12	0.39	−0.31	159.81	200.19	0.08
I14	0.37	−0.23	137.73	222.27	0.14

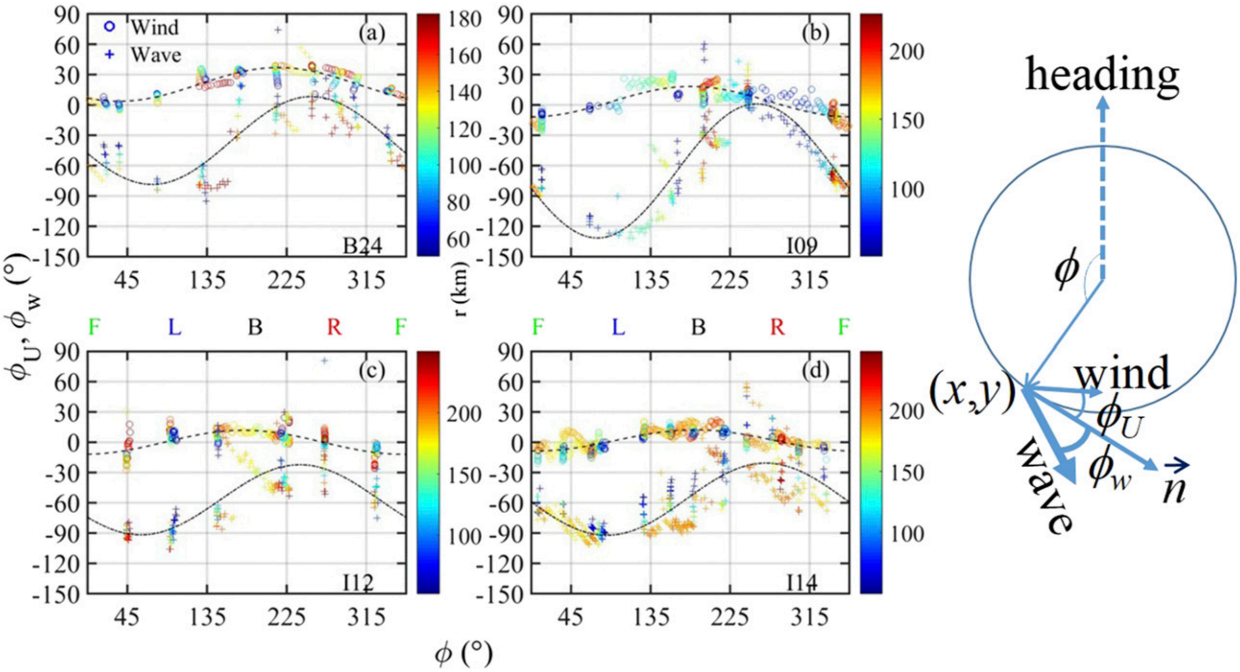

FIG. 6. Wind and wave directions ϕ_U and ϕ_w measured from the normal to the local position vector (inset) plotted against azimuth angle ϕ; the plotting markers are color-coded with r: (a) B24, (b) I09, (c) I12, and (d) I14. The least squares fitted sinusoidal curves are superimposed; the coefficients of fitting are listed in Table 4.

the component with the maximum spectral density in the 2D spectrum; the direction is referred to as the dominant wave direction. As discussed in Wright et al. (2001), Walsh et al. (2002) and Black et al. (2007), multiple spectral peaks are frequently observed, especially in the right and back sectors.

Both ϕ_U and ϕ_w show a sinusoidal variation with ϕ. The least squares fitting curves using the data with r between 50 and 200 km are superimposed in Fig. 6; the same function form [(5)] is used with the left-hand side replaced by ϕ_U or ϕ_w. The fitting coefficients for the four datasets are listed in Table 4.

The wind angles for B24 are mostly positive, meaning that the winds are veering toward the hurricane center similar to the flow pattern around a vortex. In contrast, the wind angles for I09, I12, and I14 are distributed more evenly on both sides of the position vector normal. The pattern of the azimuthal variation for I09, I12, and I14 is almost front–back or left–right antisymmetric (δ_U close to 180°; Table 4), and for B24, δ_U is about 144°. The ϕ_U maximum is at $\phi = 360° - \delta_U$.

Zhang and Uhlhorn (2012) perform a composite analysis of the surface wind inflow angles processed with a large quantity (more than 1600) of quality-controlled global positioning system (GPS) dropwindsondes deployed by aircraft on 197 flights into 18 hurricanes. The most prominent feature is also the sinusoidal azimuthal variation (their Fig. 9) with minor dependence on radial distance, hurricane translation speed, hurricane maximum wind speed, and radius of the wind speed maximum (their Figs. 6 to 8). The overall mean inflow angle is 22.6°; their convention is positive angle clockwise (CW), which is converted to positive angle CCW used in this paper. Based on Fig. 9 of Zhang and Uhlhorn (2012), the amplitude of sinusoidal azimuthal variation is about 10° to 20°, and the phase of maximum inflow angle is at about 45° to 80° CW from the hurricane heading (about R2 to F1 region in our

TABLE 4. Coefficients of fitted sinusoidal azimuthal variations of wind and wave angles (ϕ_U and ϕ_w) for the four datasets (B24, I09, I12, and I14).

	a_0	a_1	δ	$\phi_{\max}$	$\phi_{U\max}$
ϕ_U					
B24	20.31	16.65	144.42	215.58	36.66
I09	3.25	14.98	179.32	180.68	18.23
I12	−0.04	11.89	183.62	176.38	11.85
I14	1.80	10.45	174.73	185.27	12.25
	a_0	a_1	δ	$\phi_{\min}$	$\phi_{w\min}$
ϕ_w					
B24	−35.18	43.45	107.11	72.89	−78.63
I09	−65.22	66.33	105.15	74.85	−131.55
I12	−57.00	34.73	119.95	60.05	−91.73
I14	−56.38	35.77	94.65	85.35	−92.15

designation of hurricane sectors; Fig. 1 inset). Sorted with the hurricane translation speed (their Fig. 11), the phase of the maximum inflow angle is to the right and right rear of the storm (B2 to R1 sectors) for slower storms and rotates downwind toward the front of the storm (about R2 and F1 sectors) as the hurricane translation speed exceeds about 3.7 m s^{-1}. The results from the four datasets we have analyzed here (Table 4) show some similarities and differences with this composite picture. In particular, the amplitudes are in the same range. The mean value of B24 is very close to their overall mean inflow angle, but those for I09, I12, and I14 are considerably smaller. The location of the maximum inflow angle is in B2 and R1 sectors for the four cases analyzed here.

In his review of the manuscript, Jun Zhang cautions about treating the wind direction from the hurricane reconnaissance datasets as truth; the wind data used in the present analysis are the product of the NOAA HRD Real-time Hurricane Wind Analysis System (H*WIND; Powell et al. 1996; Powell and Houston 1998), which is mainly based on the stepped frequency microwave radiometer (SFMR) measurements that have no wind direction information. The surface wind direction (at 10-m elevation) from H*WIND is obtained by adding an arbitrary angle (~15°) from the flight-level wind direction. There is no systematic verification of the surface wind direction in previous literature; see also the discussion in Zhang and Uhlhorn (2012, p. 3588).

The description of how the wind velocity integrated with the wave information is minimal (Wright et al. 2001; Walsh et al. 2002), and the papers by Powell et al. (1996) and Dunion and Velden (2002) are cited. Dunion and Velden (2002) describe the derivation of vector wind information from Geostationary Operational Environmental Satellite (GOES) cloud drift analysis (the data coverage region is generally outside the 250-km circle from the hurricane center). The comparison of their results with GPS dropsonde measurements at both flight and surface (10 m) levels shows very good agreement in both speed and direction (their Tables 3 and 5). Based on Dunion et al. (2002), the GOES cloud drift analysis is also included in the H*WIND processing procedure applicable to the datasets employed in this paper. It is not clear whether the incorporation of the cloud drift analysis in the far field improves the H*WIND product in the main region of our interest [in comparison with the prior H*WIND processing described in Powell et al. (1996) and Powell and Houston (1998)].

The wave direction used in this paper from the SRA measurements is much more accurate than the wind direction from the H*WIND, so the accuracy of the wind and wave directional difference to be discussed later is limited by the uncertainty of the wind direction.

With the above caution in mind regarding the H*WIND product, the wind direction results are zoomed up in Fig. 7 for a closer examination. All data points are displayed, that is, the figure includes the measurements excluded in Fig. 6: those close to or far away from the hurricane center ($r < 50$ km or $r > 200$ km). Superimposed at the bottom of the figure are the HRD 2D wind fields representative of the four hurricane reconnaissance periods, the radii of the two red circles are 50 and 250 km. The location of maximum wind speed is marked with an x.

The hurricane wind field is frequently modeled as a vortex. The large wind speed gradient between the location of highest wind at r_m and the calm region at the hurricane center causes an inward pull (centripetal) of the wind vector. The difference of the azimuthal variation of the wind vector angles described in the discussion of Fig. 6 is likely related to the radius of wind speed maximum r_m. For B24, $r_m = 74$ km, which is considerably larger than those of I09, I12, and I14: 13, 17, and 42 km, respectively (Table 1). The observation suggests that for hurricanes with small r_m, the airflow streamlines in the main region of the hurricane coverage area (say, between $r = 50$ and 200 km) are close to circular with a significantly decreased vortex pulling effect. The wind directions veer toward the eye in the back quarter and away from the eye in the front quarter; they are more or less along the tangential of the circle at ϕ close to 90° and 270°. When r_m is large, the wind field asymmetry increases in the main region of the hurricane coverage area and the maximum inflow angle shifts downwind (from $\phi = 180°$ to 225° for the four simultaneous wind-wave datasets available for examination in this study). The vortex pulling effect is also more expansive.

In contrast to the wind direction, the wave direction veers almost always away (centrifugal) from the normal of the local position vector toward the outer edge of the hurricane (lower set of curve and markers in each panel of Fig. 6). The reasons for this veering are different between the left- and right-hand sides of the hurricane track and will be further discussed in section 3d.

Figure 8 shows the wind and wave directional difference defined as $\phi_{Uw} = \phi_U - \phi_w$. The measured results are shown with circles color-coded with the distance r from the hurricane center. The smooth solid curve is the expected result calculated from the difference between the fitted sinusoidal functions for ϕ_U and ϕ_w; we also keep the fitted curves of ϕ_U and ϕ_w in the figure for reference. The result indicates that collinear wind and wave propagations are more likely occurring in the back

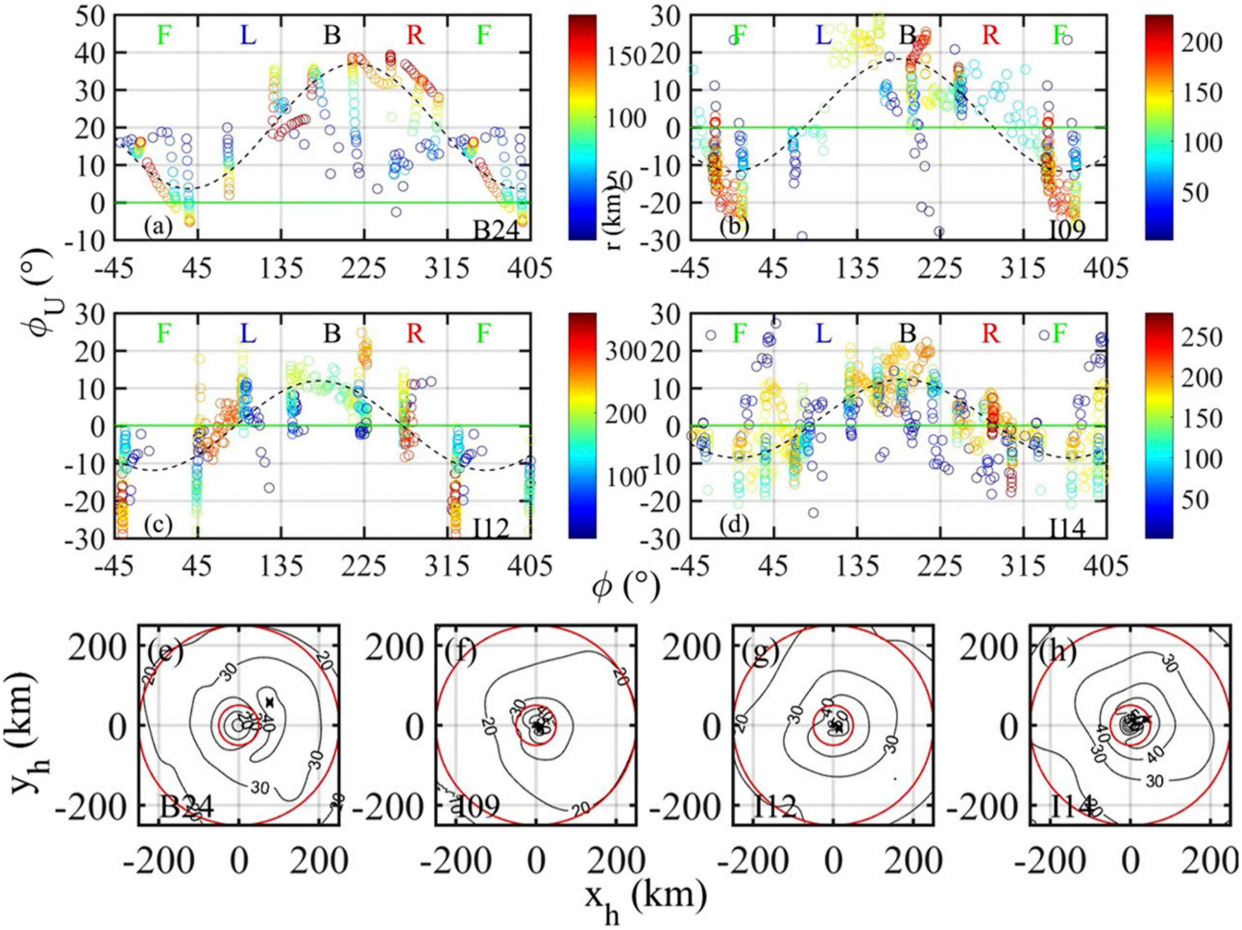

FIG. 7. Expanded view of the wind directions ϕ_U plotted against azimuth angle ϕ, the plotting markers are color-coded with r: (a) B24, (b) I09, (c) I12, and (d) I14. The bottom row shows a representative wind field for each of the four hurricane reconnaissance missions: (e) B24, (f) I09, (g) I12, and (h) I14. The radii of the two red circles are 50 and 250 km. The location of maximum wind speed is marked with an x. The coordinates are rotated such that the hurricane heading is toward the top of the page. The least squares fitted sinusoidal curves through data with $50 < r < 200$ km are superimposed in (a) to (d); the coefficients of fitting are listed in Table 4.

and right quarters. In the left quarter, wind and waves are close to perpendicular.

We can now present the comparison results of measured and modeled spectra with respect to the wind and wave directional difference. Because R_H, R_S, ϕ_U, and ϕ_w all show a sinusoidal variation with ϕ, the R_H and R_S dependence on ϕ_{Uw} is expected to be cyclical. Figure 9a shows the expected result of the height index $R_H(\phi_{Uw})$ calculated from the sinusoidal fitted curves of the relevant variables (R_H, ϕ_U, and ϕ_w) derived for the four datasets. Figures 9b to 9e show the corresponding actual observations. To aid the comparison, color markers matching the color maps in Figs. 9b–e are added on the trajectories in Fig. 9a to indicate the four hurricane quarters. The locations corresponding to $\phi = 0°$ (360°) and 15° (375°) are marked with x and +, respectively, to show the direction along the trajectory of $R_H(\phi_{Uw})$ as an observer moves inside hurricane CCW along a path with increasing azimuth angle ϕ. Similar to Fig. 5a, the color map is arranged such that increasing ϕ corresponds approximately to increasing wave age (roughly in the order of B, R, F, and L; color-coded blue, cyan, yellow, and red, respectively).

The results from analyzing the four datasets consistently show small ϕ_{Uw} (wind and wave collinear) and R_H close to 1 (good agreement between modeled and measured spectra) in the back and right quarters (blue and cyan colors) and wider angles between wind and wave propagations accompanying larger differences between measurement and model in the left and front quarters (yellow and red colors).

As illustrated in Fig. 10, presented in the same format as Fig. 9, the spectral index R_S shows a similar pattern as that of R_H. In this case, R_S close to 0 represents good

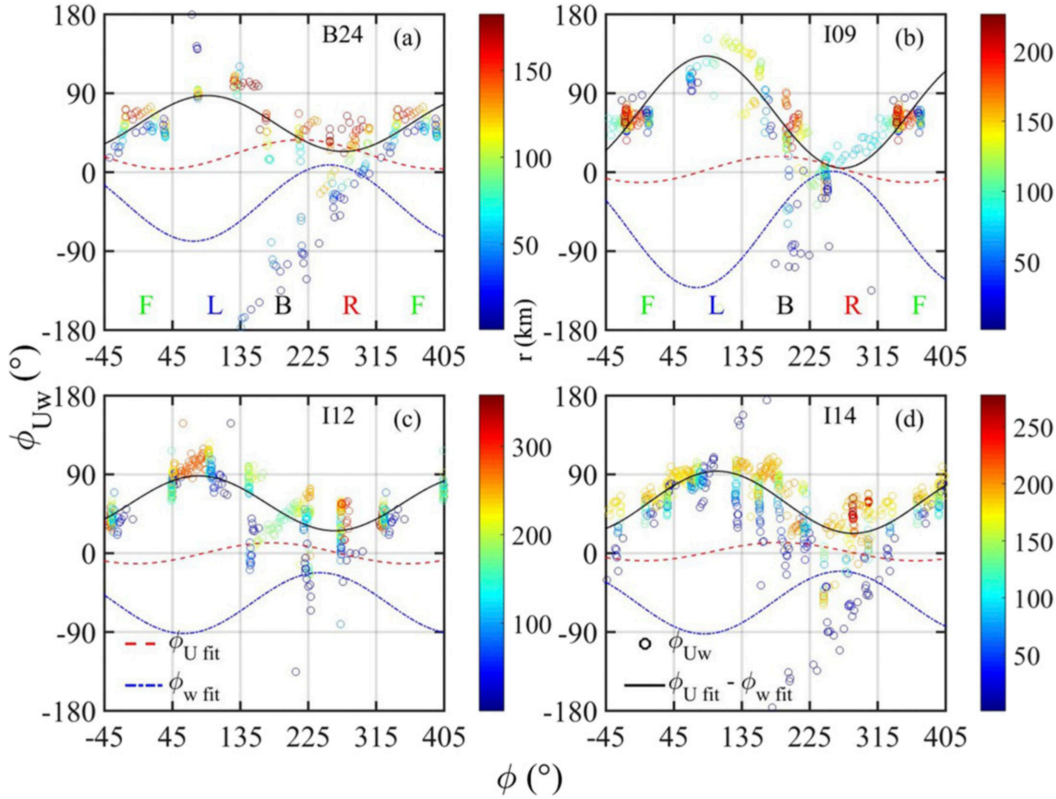

FIG. 8. The wind and wave directional difference ϕ_{Uw} plotted against azimuth angle ϕ; the plotting markers are color-coded with r: (a) B24, (b) I09, (c) I12, and (d) I14. The curve calculated from the difference of the least squares fitted sinusoidal functions of wind and wave angles are shown with solid curves. For reference, the fitted functions of ϕ_U and ϕ_w are also displayed with dashed and dashed–dotted curves.

agreement between modeled and measured spectra. Again, the better agreement is found in the back and right quarters with smaller values of R_S and ϕ_{Uw}; degraded agreement occurs in the left and front quarters with larger values of R_S and ϕ_{Uw}.

d. *Causes of directional difference of hurricane winds and waves*

A characteristic feature of the ocean response to a moving storm is the strongly biased mixed layer current to the right side of the hurricane track (in Northern Hemisphere). It occurs because the wind stress vector turns CW in time on the right-hand side of the track and CCW on the left-hand side of the track (e.g., see Fig. 4 of Fan et al. 2009a). For typical hurricane dimensions and translation speeds, the rate of turning of the stress vector on the right-hand side is comparable to the turning rate of an inertial motion. Hence, there is a near-resonant coupling of the wind stress and the wind-driven, near-inertial oscillation of the mixed layer velocity (Price 1981).

On the left-hand side of the hurricane, the ocean currents are much weaker and do not show a large angle from the wind direction. However, unlike the wave system on the right-hand side of the storm that is dominated by locally generated wind seas, the waves in the left sector are dominated by the preexisting oscillations consisting of waves propagated from an upstream area with significantly different directional property with the local wind.

Figure 11a depicts a conceptual sketch showing that the upstream waves in the left sector at time t_2 propagated from wind seas from the front sector at an earlier time t_1. In this simple sketch, it is assumed that waves propagate in straight lines and they can form a very wide angle from the local wind at t_2. For a more realistic scenario with continuous wind modification along the way from t_1 to t_2, the resulting wave direction becomes ~90° to the right of the local wind vector in the left sector of the hurricane.

As noted earlier, the complicated spatial structure of the wind and wave directional difference observed in the hurricane reconnaissance datasets has been discussed in great detail but in qualitative terms (e.g., Wright et al. 2001; Young 2006; Black et al. 2007). For example, Figs. 11b and 11c reproduce Figs. 9 and 10 of Black et al. (2007). The

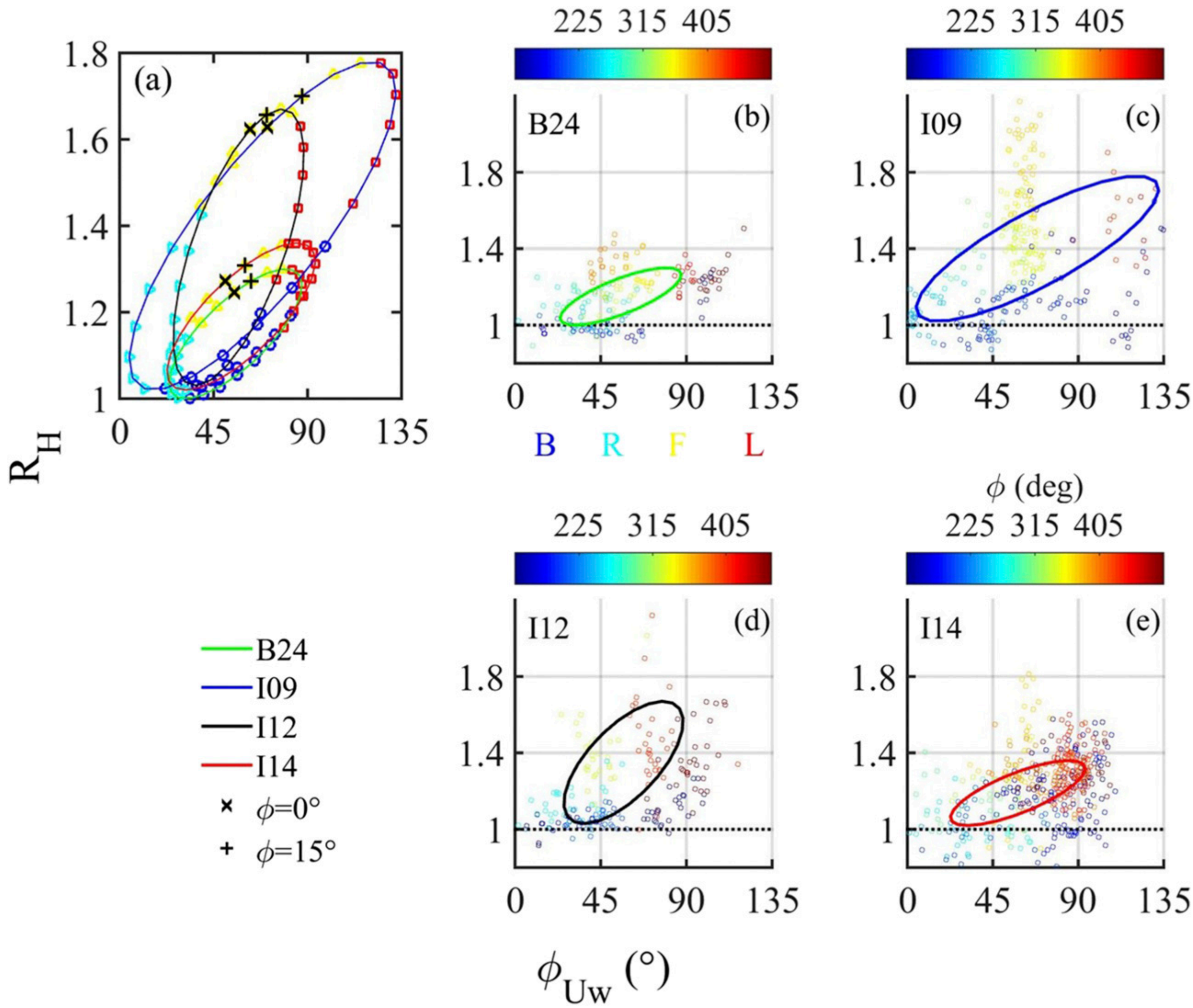

FIG. 9. (a) The cyclic pattern of the R_H dependence on ϕ_{Uw} calculated with the least squares fitted functions of R_H, R_S, ϕ_U, and ϕ_w for the four hurricane reconnaissance datasets; the corresponding field observations are shown in (b) B24, (c) I09, (d) I12, and (e) I14. To aid the comparison, color-coded markers matching the color bar in (b)–(d) are added on the curves in (a) to identify the four quarters of the hurricane coverage area; markers x and + indicate $\phi = 0°$ (360°) and 15° (375°) to show the direction of the cyclic trajectories.

former shows the primary wave propagation directions with solid black ''streamlines'' derived from Bonnie 1998 measurements, and the latter displays 12 2D wavenumber spectra of Ivan 2004 measured at about 80 km from the hurricane center. These figures effectively summarize the various delicate features of surface waves in different hurricane sectors, such as the confused and multimodal seas in the right and back sectors and the wide angles between wind and wave propagations, especially in the left sector. Figure 11d is a conceptual sketch revising Fig. 1c of Hwang (2016) to give a much simplified representation of the multimodal wave patterns on the right and back sectors and somewhat less complicated wave conditions on the front and left sectors of the hurricane.

The analysis presented in section 3c makes use of the precise radial and azimuthal information in the hurricane reconnaissance datasets to construct a quantitative model of the wind and wave directional difference. These results may be useful for in-depth and quantitative analyses of the wind–wave interaction in hurricane conditions.

e. Implications on wind–wave interaction

The oblique waves propagated from the upstream area are called ''swell'' in some publications. We refrain

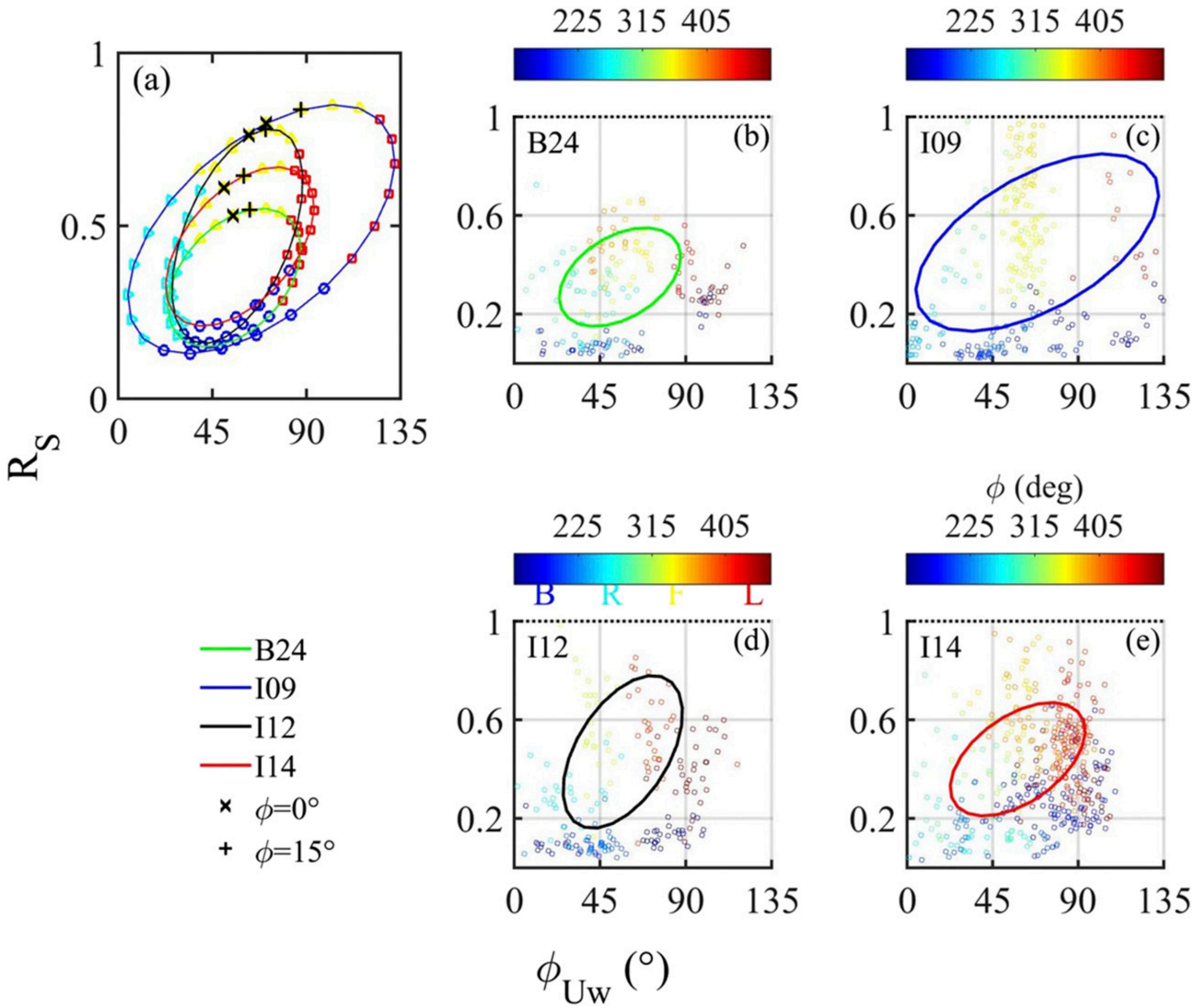

FIG. 10. As in Fig. 9, but for R_S.

from such a designation because these upstream waves are propagating much slower than the local winds, and they are still under strong local wind modification. They are thus dynamically very different from the more conventional definition of the swell that moves considerably faster than the wind ($c_p > \sim 1.25U_{10}$), for which there is little interaction between the wind and swell systems. The upstream waves in hurricanes actually continue to interact with the local wind and dominate the spectrum, with a wave age $c_p/U_{10} = 1/\omega_\#$ typically between 0.3 and 1.0 in the left quarter of the hurricane main region (see Fig. 14 of Hwang and Fan 2017).

The hurricane reconnaissance wave spectra in the left-hand sector are usually monomodal despite the large wind and wave angles (Fig. 8), as illustrated in Figs. 6 to 9 of Wright et al. (2001) and Fig. 10 of Black et al. (2007). The monomodal wave spectra in the left sector strongly indicate that the oblique wave system absorbs the lion's share of the local wind input. The feature of oblique waves monopolizing the local wind input occurring even when the winds and dominant waves are almost perpendicular reflects the observations that existing background waves steer away the surface roughness and wind stress from the wind direction (e.g., Hwang and Shemdin 1988; Grachev et al. 2003). This feature needs to be a serious consideration in modeling wind-wave generation in the presence of background waves or under unsteady wind forcing conditions (either in direction or in speed).

We reemphasize that dominantly monomodal spectra are observed in the sectors with large differences between the wind and wave angles, indicating that preexisting oblique waves effectively grab the local wind input. The directionally multimodal spectra are in fact frequently

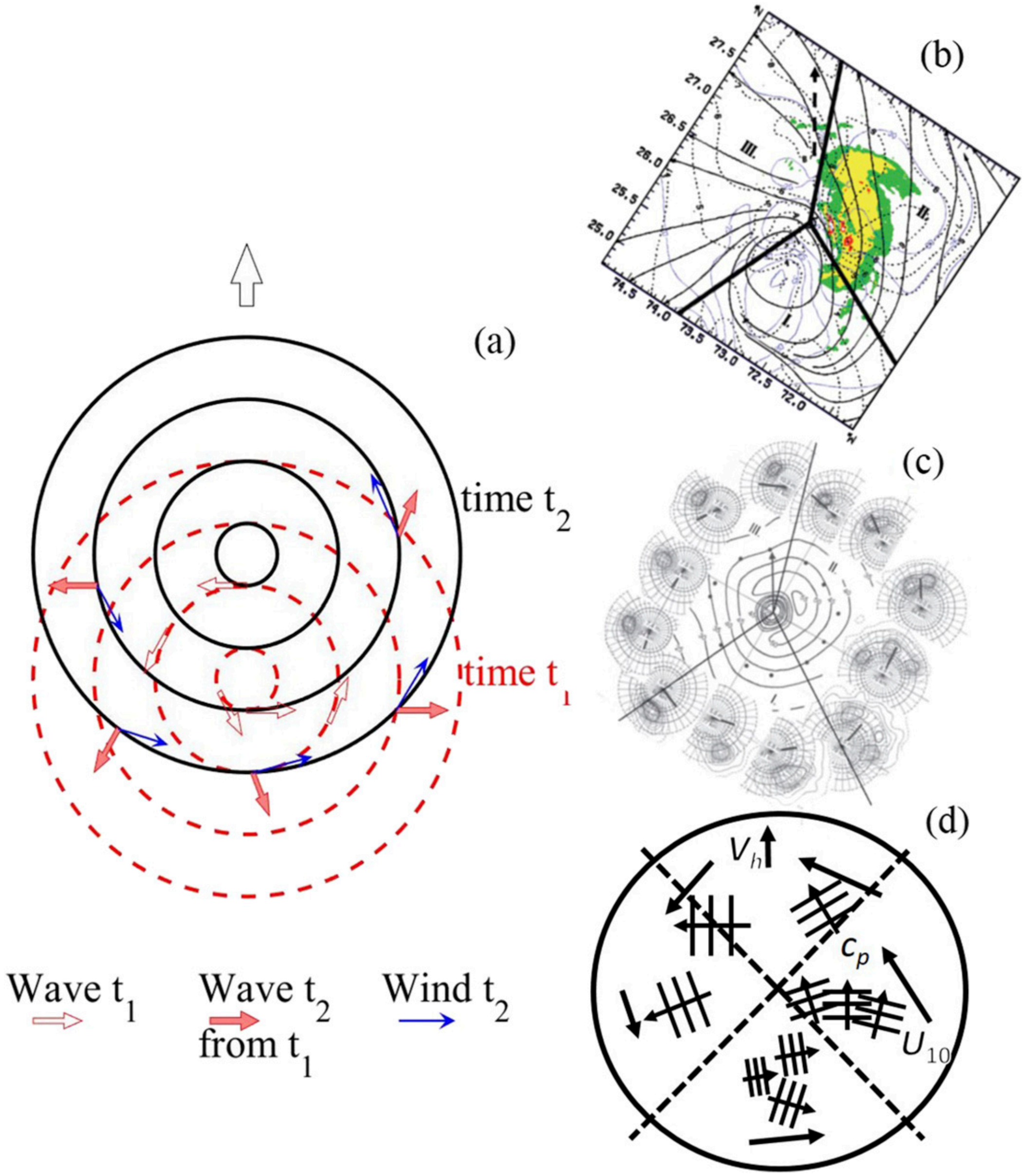

FIG. 11. (a) A conceptual sketch illustrating the wave propagation from time t_1 (open red arrows) to time t_2 (filled red arrows) at several locations inside a hurricane, and the resulting directional difference from the wind vectors at time t_2 (blue arrows); (b) analysis of SRA primary wave direction (Bonnie 1998) shown as solid black streamlines (Black et al. 2007; Fig. 9); (c) 12 2D wave spectra (Ivan 2004) measured by the SRA near 80 km from the hurricane center, the location of each spectrum is shown as a black dot on the figure (Black et al. 2007; Fig. 10); and (d) a conceptual sketch (revised Fig. 1c of Hwang 2016) showing the general wave patterns in different sectors of a hurricane.

observed in the regions with almost collinear wind and dominant wave propagations, that is, in the neighborhood of B1, B2, and R1 sectors (Fig. 1, inset), as exemplified by the 2D wavenumber spectra (Fig. 12) of the four samples illustrated in Figs. 2 and 3. Many more representative spectra in different sectors are displayed in Figs. 6 to 9 of Wright et al. (2001). Additional discussion on the subject can be found in, for example, Wright et al. (2001), Walsh et al. (2002), Moon et al. (2003), Young (2006), Fan et al. (2009a,b), Holthuijsen et al. (2012), Esquivel-Trava et al. (2015), and Fan and Rogers (2016). The analysis presented in section 3c offers a quantitative model summarizing these qualitative descriptions. The result is also useful for wave model simulations in hurricane conditions, for

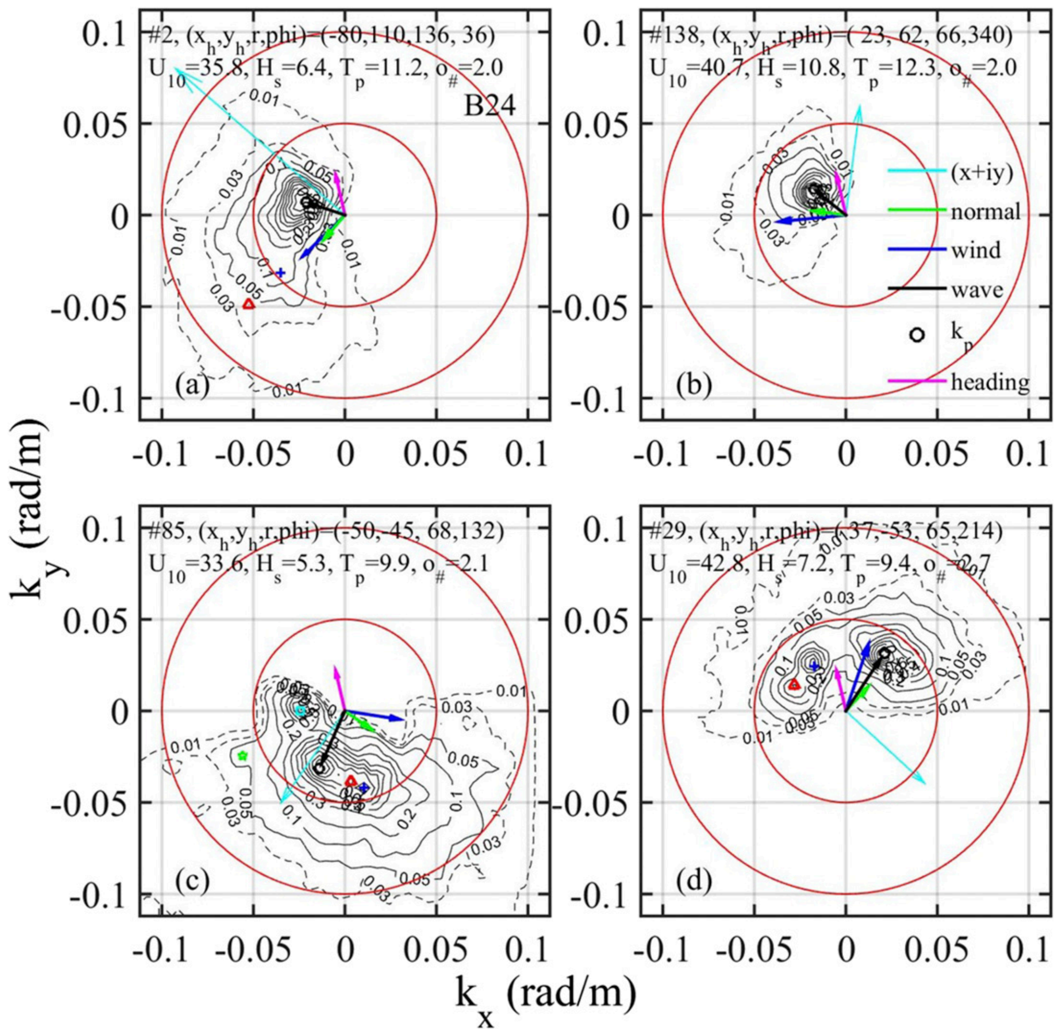

FIG. 12. This figure shows the normalized SRA 2D wavenumber spectra, the corresponding 1D spectra processed from which are shown in Figs. 2 and 3. Also illustrated with arrows of different colors as labeled in the legend are the position vector proportional to its distance from the hurricane center, the position vector normal, the wind and dominant wave vectors, and the hurricane heading. The location of the local spectral peaks are shown in descending order (up to five local peaks) with symbols circle, plus, triangle, square and penta-star. The Earth coordinates [east (E), north (N), west (W), and south (S)] are used. The position vector (x_h, y_h), and (r, ϕ) rotated with reference to the hurricane heading are shown in the upper text string; wind speed, wave height, wave period, and dimensionless frequency are shown in the lower text string.

example, for providing a framework to specify the effective wind stress vectors in different locations of the hurricane coverage area.

f. Spectral slope and Doppler frequency shift

The measured spectral slope in the high-frequency region varies considerably. For example, the range in the D model database processed with frequency–wavenumber spectral analysis is between about −3.5 and −5 (Donelan et al. 1985). As discussed in section 2b, Young (1998) shows a scatterplot of the spectral slopes from his analysis of hurricane-generated directional wave spectra collected over a 16-yr period. The data are shown in Fig. 13a. Most of the spectral slopes fall between −3 and −6; the mean value is −4.56. The results of the spectral slope analysis using the wave data from INTOA show similar range, and they are included in the figure for comparison.

Attempts to correlate s with various INTOA wind and wave parameters, including U_{10}, H_s, T_p, their dimensionless combinations $\omega_\#$ and $\eta_\#$, and several swell–sea ratios, did not yield concrete results. It is deduced that s needs to be treated as a stochastic random variable. Figure 13b shows the probability density functions (pdfs) $p(s)$ of the two datasets; only wind-sea conditions are

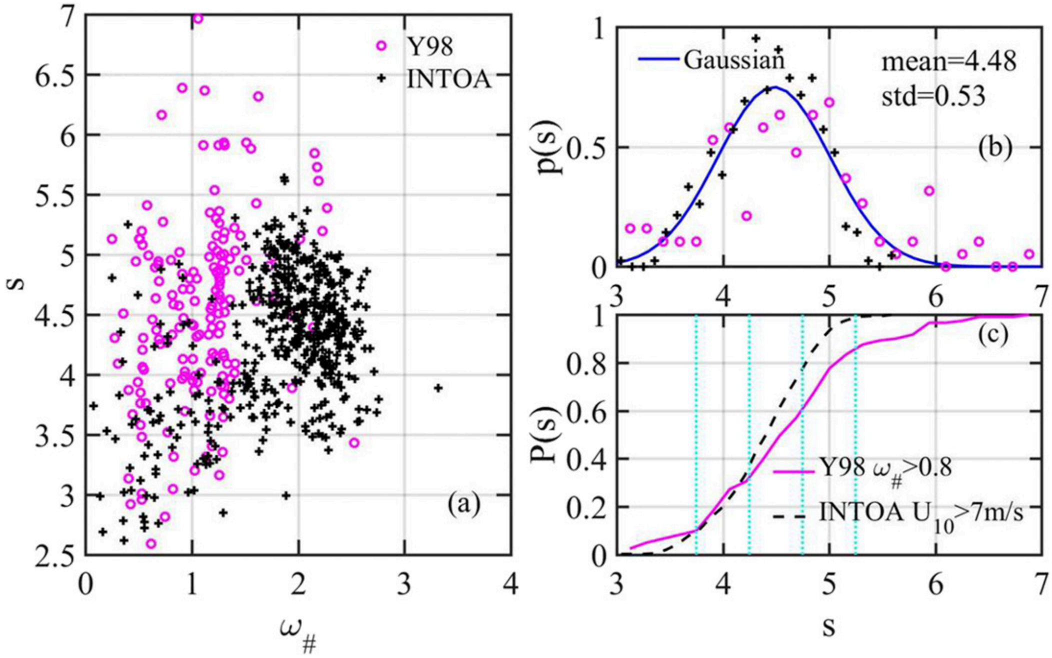

FIG. 13. (a) The spectral slope magnitude s of hurricane-generated waves (labeled Y98) processed from directional buoy measurements (Young 1998); results from INTOA wave spectral analysis are superimposed for comparison, (b) the pdf $p(s)$ of the two datasets, the superimposed Gaussian curve is computed with the combined mean and standard deviation displayed at the upper-right corner, and (c) the CDF $P(s)$ of the two datasets.

included in the pdf computation. The pdf is close to the Gaussian distribution. The superimposed Gaussian curve is computed with the combined mean and standard deviation of 4.48 and 0.53, respectively.

Figure 13c shows the cumulative distribution functions (CDFs) $P(s)$ of the two datasets (wind-sea subpopulations only). The cumulative fractions in the ranges of $s = 4 \pm 0.25$, 4.5 ± 0.25, and 5 ± 0.25 are, respectively, 21%, 26%, and 31% for the Young (1998) dataset and 22%, 43%, and 23% for the INTOA dataset. There is clearly a need for a spectral representation that can accommodate the observed spectral slope variability (appendix).

The wide range of the observed spectral slopes in the neighborhood of the spectral peak region ($1.5\omega_p$ to $3\omega_p$ or $2\omega_p$ to $4\omega_p$) is unlikely caused by the Doppler frequency shift, which is a serious issue for the study of short-scale surface waves that serve as the emission or scattering roughness in microwave remote sensing of the ocean. Hwang (2006b) presents an analysis of the Doppler frequency shift from background currents. His analysis is briefly summarized below.

For a given wavenumber spectrum $S(k)$, the observed frequency spectrum $S(\omega)$ is given as

$$S(\omega)\, d\omega = S(k)\, dk. \qquad (6)$$

In the presence of ocean surface vector current $\mathbf{u}$, the observed (encounter) frequency ω is related to the wavenumber k by

$$\omega = (gk + \tau k^3)^{0.5} + \mathbf{u} \cdot \mathbf{k}, \qquad (7)$$

where τ is surface tension, which can be ignored for our application to wave components near the spectral peak, and boldfaced variables ($\mathbf{u}$ and $\mathbf{k}$) represent vectors. Deep-water wave condition is assumed in (7). The surface current can be decomposed into mean current U_c, wave orbital velocity U_w from longer waves (compared to the wave component k considered), and surface wind drift U_d.

For the worst-case scenario of collinear wind and wave propagations and assuming that the thin-layered wind drift produces frequency shift equal to the mean current of the same magnitude, the Jacobian in (6) can be written as

$$J = \left|\frac{dk}{d\omega}\right| = \left|\frac{1}{c_g + u}\right| = \left|\frac{1}{c_g + U_o\cos\theta + U_c + U_d}\right|, \qquad (8)$$

where U_o is the amplitude of the long-wave orbital velocity approximated by a sinusoidal oscillation $\cos\theta$.

Assuming that the surface wind drift is 2% of wind speed, Fig. 14 shows several examples of calculations

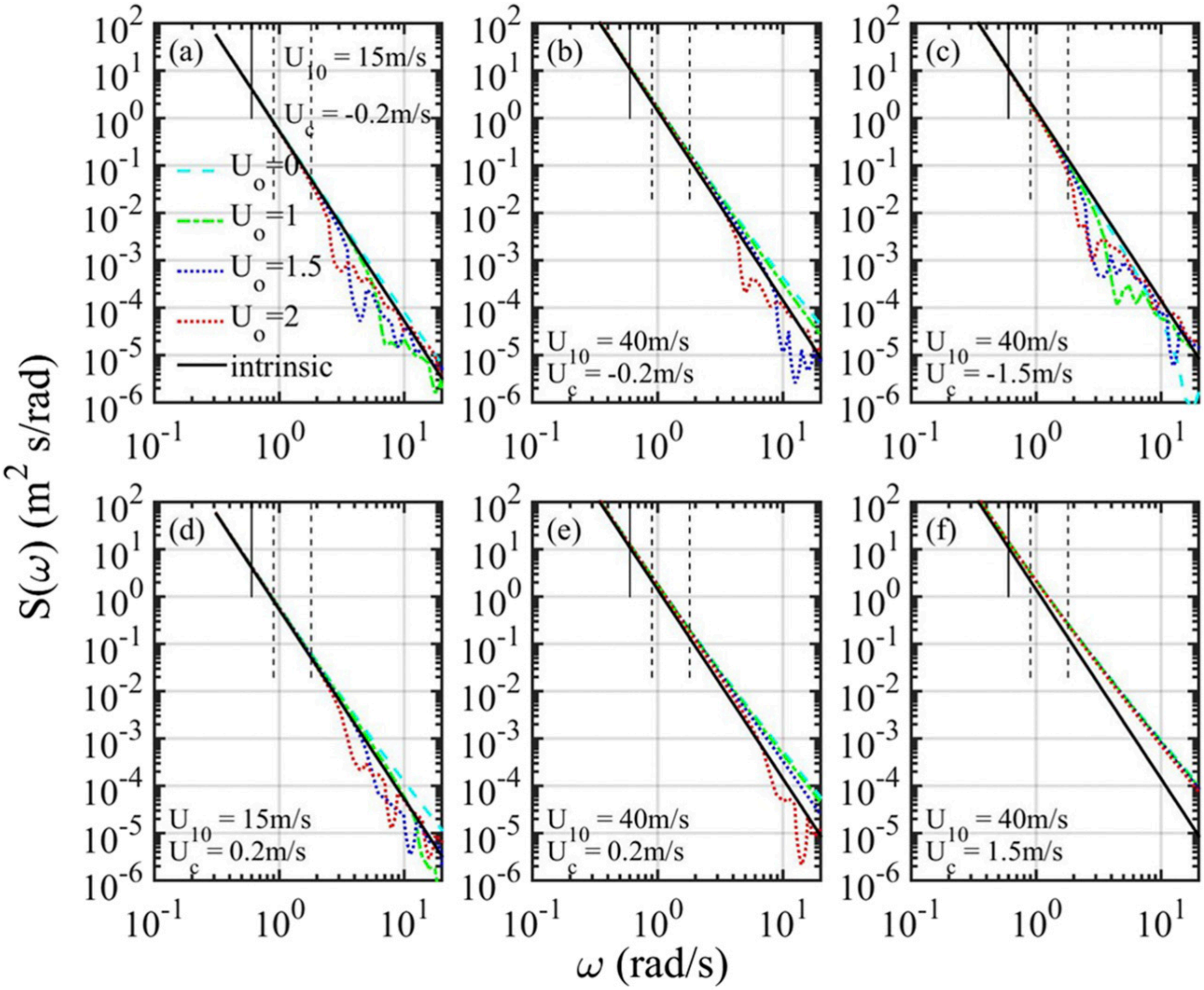

FIG. 14. Examples of Doppler frequency shift computations. For each panel, the black solid line is the intrinsic $k^{-2.5}$ or ω^{-4} function, and four color curves represent $U_o = 0, 1, 1.5$, and $2\,\mathrm{m\,s^{-1}}$ with wind drift $U_d = 0.02U_{10}$. Each of the six panels is calculated with different U_{10} and U_c (both $\mathrm{m\,s^{-1}}$): (a) $U_{10} = 15$, $U_c = -0.2$; (b) $U_{10} = 40$, $U_c = -0.2$; (c) $U_{10} = 40$, $U_c = -1.0$; (d) $U_{10} = 15$, $U_c = 0.2$; (e) $U_{10} = 40$, $U_c = 0.2$; and (f) $U_{10} = 40$, $U_c = 1.5$. See the main text for further details.

integrated over integer cycles of $\cos\theta$ orbital velocity fluctuations with various U_{10}, U_c, and U_o. For each panel, the black solid line is the intrinsic $k^{-2.5}$ or ω^{-4} function, and four color curves represent $U_o = 0$, 1, 1.5, and $2\,\mathrm{m\,s^{-1}}$ with wind drift $U_d = 0.02U_{10}$. Each of the six panels is calculated with different U_{10} ranging from 10 to $50\,\mathrm{m\,s^{-1}}$ and $|U_c|$ ranging from 0 to $2\,\mathrm{m\,s^{-1}}$. If wind and waves are not collinear, the effective current magnitude for the Doppler frequency shift computation is reduced by a factor equal to $\cos\phi_x$, where ϕ_x is the angle between the wave and current vectors.

The hurricane reconnaissance observations show that the ω_p range is typically between about 0.4 and 0.7 $\mathrm{rad\,s^{-1}}$; the range of $4\omega_p$ is thus between about 1.5 and 3 $\mathrm{rad\,s^{-1}}$. For an illustration of the effect on spectral slope determination, line segments are added in the figure for an example with $\omega_p = 0.6\,\mathrm{rad\,s^{-1}}$ (shown with a short solid line segment in each panel), the region between $1.5\,\omega_p$ and $3\,\omega_p$ are marked with a pair of short dashed lines. From the sample computations shown in Fig. 14, it can be deduced that meaningful changes of the spectral slope from the effect of Doppler frequency shift requires very unusual surface current conditions such as that encountered in the Gulf Stream core region ($U_c \approx \pm 2\,\mathrm{m\,s^{-1}}$) or in the Gulf of Mexico Loop Current ($U_c \approx \pm 1.5\,\mathrm{m\,s^{-1}}$, depicted in the right column; Figs. 14c,f). For more common ocean current conditions, such as those shown in the left two columns with $U_c \approx \pm 0.2\,\mathrm{m\,s^{-1}}$ (Figs. 14a,b,d,e), the spectral slope modification is rather insignificant compared to variation in the field observations.

4. Summary

In this paper, the wave spectra measured inside tropical cyclones in four hurricane reconnaissance missions are analyzed and compared with three wind-wave spectral models. Indices to quantify the agreement between model and measurement are given by $R_H = H_{sm}/H_s$ and $R_S = \sigma_S^{0.5}/H_s$. In the main region of the hurricane coverage (tentatively given as about 50 to 200 km from the hurricane center), both indices show mild dependence on the radial distance from the hurricane center and significant sinusoidal dependence on the azimuth angle referenced to the hurricane heading (Fig. 5).

Similar sinusoidal azimuthal variation and mild radial dependence are found in the wind and wave directions ϕ_U and ϕ_w measured from the normal of the local position vector (Fig. 6). As a result, the wind and wave directional difference ϕ_{Uw} in the main region of the hurricane coverage area can be approximated by a sinusoidal function (Fig. 8). The cyclical patterns of the R_H and R_S dependence on ϕ_{Uw} observed in the hurricane reconnaissance datasets can be described very well by the analytical curves derived from the sinusoidal fitting functions of R_H, R_S, ϕ_U, and ϕ_w (Figs. 9, 10).

The hurricane reconnaissance 2D wave spectra show repeatedly that monomodal spectra are observed in the sectors with large wind and wave directional differences, indicating that preexisting oblique waves effectively absorb the local wind input. The multimodal spectra are in fact more likely observed in the region with almost collinear propagations of the local winds and dominant waves, that is, in the neighborhood of B1, B2, and R1 sectors, as illustrated in Fig. 12 and many other representative 2D spectra displayed in Figs. 6 to 9 of Wright et al. (2001). Figures 9 and 10 of Black et al. (2007), reproduced as Figs. 11b and 11c, succinctly summarize many of the delicate features of the wind and wave directional properties. The analysis presented in section 3c yields quantitative models summarizing these qualitative descriptions. These quantitative functions are useful for understanding the wind–wave interactions and for prescribing the effective wind stress vectors inside hurricanes in numerical wave simulations under hurricane conditions.

We also present a discussion on the wide range of the spectral slopes observed in both hurricane and nonhurricane field data. Analytical computations (Fig. 14) indicate that the effect of Doppler frequency shift from background currents is unlikely the cause of the observed spread of the spectral slopes determined from wave components close to the peak region from 1.5 ω_p to 3 ω_p (Donelan et al. 1985) or 2 ω_p to 4 ω_p (Young 1998). Efforts to search for a correlation between the spectral slope and various wind and wave parameters or swell–sea ratios have not yielded concrete results. The negative outcome in finding a correlation suggests that the spectral slope needs to be treated as a stochastic random variable. Complementing the existing wind-wave spectral models that prescribe a fixed spectral slope of either −4 or −5, a general spectral model with its spectral coefficients accommodating a variable spectral slope is introduced (appendix). The accurate determination of the spectral slope is important in the understanding of the wave dynamics in the equilibrium range that has significant implications in many ocean surface processes such as wave breaking, whitecaps, and surface roughness (e.g., Phillips 1985).

Acknowledgments. This work is sponsored by the Office of Naval Research (Funding Document N0001416WX00044) and CONACYT (project 155793, RugDiSMar; recipient F. J. Ocampo-Torres, CICESE). The INTOA field experiment was supported by CONACYT (SEP-2003-C02-44718; recipient F. J. Ocampo-Torres, CICESE). We are grateful for the careful preservation of the SRA datasets and supporting information provided by Ed Walsh, and the service of HRD wind archive maintained in the HWIND legacy data site (http://www.rms.com/perils/hwind/legacy-archive/). Ed Walsh is the person most deserving of the credit for the works coming out from these datasets but had declined coauthorship after Hwang and Walsh (2016) because he has retired and values his freedom to do whatever he pleases after retirement. We are grateful for the contributions by him and many others behind the scene to make it possible for us to get a few rare glimpses of the winds and waves inside hurricanes. We also thank Jun Zhang and an anonymous reviewer for their many comments and suggestions to improve the quality of this paper. Datasets used in this analysis are given in the references cited. The processing codes and data segments can also be obtained by contacting the corresponding author. U.S. Naval Research Laboratory Publication Number JA/7260-17-0051.

APPENDIX

Wind-Wave Spectral Models

A wave spectrum describes the quasi-periodic nature of the ocean surface oscillations. In this paper, we present a brief summary of several milestones marking the long effort of spectral model development of wind-generated wave: Pierson and Moskowitz (1964), referred to as the P model; Hasselmann et al. (1973, 1976), referred to as the J model; Donelan et al. (1985), referred to as the D model; and Young (2006), referred to as the Y model.

After the discussion of published spectral models, we also propose a general model referred to as the G model. The spectral slope in the high-frequency portion of the spectrum is −5 for the P and J models, −4 in the D model, and variable for the Y and G models. The Y model, however, does not resolve the spectral slope dependence on the associated spectral coefficients, and the applications rely on the spectral coefficients developed by the D or J spectral models, so its legitimate use remains for −4 or −5 slope.

The P model (Pierson and Moskowitz 1964) is given as

$$S(\omega) = \alpha_P g^2 \omega^{-5} \exp\left[-\beta_P\left(\frac{\omega}{\omega_0}\right)^{-4}\right], \qquad \text{(A1)}$$

where $\alpha_P = 8.10 \times 10^{-3}$, $\beta_P = 0.74$, $\omega_0 = g/U_{19.5}$, and $U_{19.5}$ is the wind speed measured on the weather ship with the sensor elevation at 19.5 m above mean sea level (Pierson 1964).

The J model (Hasselmann et al. 1973, 1976) is given as

$$S(\omega) = \alpha_J g^2 \omega^{-5} \exp\left[-\frac{5}{4}\left(\frac{\omega}{\omega_p}\right)^{-4}\right]\gamma_J^{\Gamma_J};$$

$$\Gamma_J = \exp\left[-\frac{(\omega-\omega_p)^2}{2\sigma_J^2\omega_p^2}\right], \qquad \text{(A2)}$$

where ω_p is the spectral peak frequency, α_J is no longer a constant but varies with the wind fetch x_f, and

$$\alpha_J = 0.076 x_\#^{-0.22}, \qquad \text{(A3)}$$

where $x_\# = x_f g U_{10}^{-2}$ is the dimensionless fetch. The dependence on fetch can be converted to the dependence on wave age ($c_p U_{10}^{-1} = \omega_\#^{-1}$, where c_p is the wave phase speed of the spectral peak component and $\omega_\# = \omega_p U_{10} g^{-1}$ is the dimensionless spectral peak frequency) using their wave frequency growth function $\omega_\# = 21.99 x_\#^{-0.33}$; (A3) can be rewritten as

$$\alpha_J = 9.88 \times 10^{-3} \omega_\#^{0.66}. \qquad \text{(A4)}$$

The two peak enhancement parameters γ_J and σ_J are also expected to be dependent on fetch or wave age, but the JONSWAP data scatter is very large. In practice, the mean values $\gamma_J = 3.3$, $\sigma_a = 0.07$, and $\sigma_b = 0.09$ are frequently employed (the J model defines the peak width σ_J as σ_a and σ_b for $\omega < \omega_p$ and $\omega \geq \omega_p$, respectively).

After reviewing more than a dozen datasets, Hasselmann et al. (1976) suggest the power function dependence for the model parameters. From the average values listed in the last entry of their Table 1, the following formulas are derived:

$$\alpha_{J2} = 7.33 \times 10^{-3} \omega_\#^{0.87}, \qquad \text{(A5)}$$

$$\gamma_{J2} = 2.29 \omega_\#^{0.32}, \qquad \text{(A6)}$$

$$\sigma_{aJ2} = 9.85 \times 10^{-2} \omega_\#^{-0.32}, \quad \text{and} \qquad \text{(A7)}$$

$$\sigma_{bJ2} = 1.05 \times 10^{-1} \omega_\#^{-0.16}. \qquad \text{(A8)}$$

The D model (Donelan et al. 1985) is given as

$$S(\omega) = \alpha_D g^2 \omega_p^{-1} \omega^{-4} \exp\left[-\left(\frac{\omega}{\omega_p}\right)^{-4}\right]\gamma_D^{\Gamma_D};$$

$$\Gamma_D = \exp\left[-\frac{(\omega-\omega_p)^2}{2\sigma_D^2\omega_p^2}\right]. \qquad \text{(A9)}$$

The model parameters obtained from their data are

$$\alpha_D = 0.006 \omega_\#^{0.55}; \quad 0.83 < \omega_\# < 5, \qquad \text{(A10)}$$

$$\gamma_D = \begin{cases} 1.7, & 0.83 < \omega_\# < 1 \\ 1.7 + 6.0 \log \omega_\#, & 1 \leq \omega_\# < 5 \end{cases}, \quad \text{and} \qquad \text{(A11)}$$

$$\sigma_D = 0.08(1 + 4\omega_\#^{-3}); \quad 0.83 < \omega_\# < 5. \qquad \text{(A12)}$$

The Y model (Young 2006) is given as

$$S(\omega) = \alpha_Y g^2 \omega_p^{-(5+s)} \omega^{-s} \exp\left[-\frac{s}{4}\left(\frac{\omega}{\omega_p}\right)^{-4}\right]\gamma_Y^{\Gamma_Y};$$

$$\Gamma_Y = \exp\left[-\frac{(\omega-\omega_p)^2}{2\sigma_Y^2\omega_p^2}\right]. \qquad \text{(A13)}$$

Young (2006) does not resolve the spectral slope dependence on the associated spectral coefficients α_Y, γ_Y, and σ_Y, so its legitimate application is still restricted to $s = 4$ or 5 using the α, γ, and σ by Donelan et al. (1985) or Hasslemann et al. (1973, 1976), thus resulting in identical outcome as that of the D or J model.

The G model also accepts a variable spectral slope and is given as

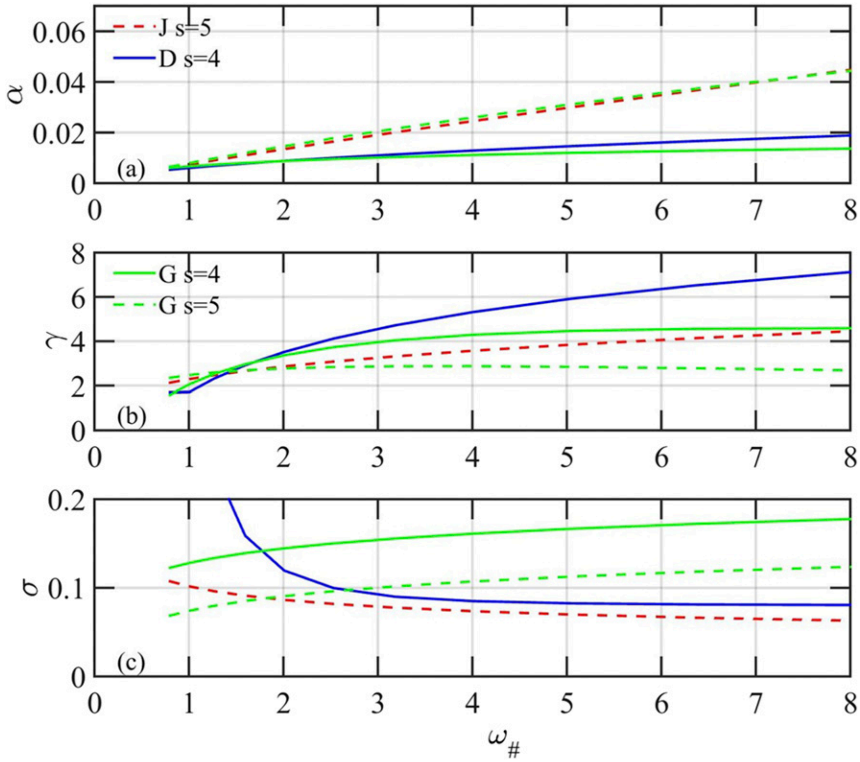

FIG. A1. Comparison of (a) α, (b) γ, and (c) σ for the J (red), D (blue), and G (green) spectral models: $s = 4$ (solid) and 5 (dashed).

$$S(\omega) = \alpha_G g^2 \omega_p^{-5} \zeta^{-s} \exp\left[-\left(\frac{\zeta}{K}\right)^{-\beta_G}\right] \gamma_G^{\Gamma_G};$$

$$\Gamma_G = \exp\left[-\frac{(1-\zeta)^2}{2\sigma_G^2}\right]; \quad \zeta = \frac{\omega}{\omega_p}, \tag{A14}$$

where K is a scaling factor such that the peak of $S(\omega)$ is at ω_p. Setting $dS/d\omega = 0$, one obtains $K = (s/\beta_G)^{1/\beta_G}$. In the G model, the associated spectral parameters vary with s as detailed below; the spectral slope at the high-frequency portion is no longer restricted to -4 or -5. The P, J, D, and Y models are subsets of the G model, that is, for the P model, $[s, \beta_G, \gamma_G] = [5, 4, 1]$; for the J model, $[s, \beta_G] = [5, 4]$; for the D model, $[s, \beta_G] = [4, 4]$; and for the Y model, $[\beta_G] = [4]$.

In practical application, it turns out that the impact of varying β_G in (A14) is relatively small in comparison to varying α_G, γ_G, and σ_G. Furthermore, the nonlinear curve fitting procedure becomes more complicated as the number of fitting variables increases, thus placing higher demand on the quality and quantity of wave spectra used for analysis. Limited by the spectral resolution in the present study, $\beta_G = 4$ is adopted following the examples of the P, J, D, and Y models. From this point on, the subscript letters associated with α, γ, and σ for different models are dropped unless clarification is necessary.

The spectral parameters for the G model are estimated in two steps. The first step uses the combined data of spectral parameters processed from the INTOA wave spectra with published results of JONSWAP (Hasselmann et al. 1973, 1976) and Donelan et al. (1985). This combination is necessary because the INTOA data range of $\omega_{\#}$ is rather limited: from 1.4 to 3.3 for $U_{10} > 7\,\mathrm{m\,s^{-1}}$ but mostly between 1.5 and 2.7. For the INTOA data processing, the MATLAB function lsqcurvefit is used to obtain the optimal values of α, γ, and σ simultaneously by minimizing the mean-square errors between each measured wave spectrum and the fitted curve. Because of the wide range of the $S(\omega)$ magnitude due to the ζ^{-s} dependence, least squares fitting procedure works much more efficiently on the scaled function $S_s(\omega) = \zeta^s S(\omega)$.

The combined data yield

$$\alpha_1 = A_\alpha \omega_{\#}^{a_\alpha}, \tag{A15}$$

$$\gamma_1 = A_\gamma + a_\gamma \log(\omega_{\#}), \quad \text{and} \tag{A16}$$

$$\sigma_1 = A_\sigma + a_\sigma \log(\omega_{\#}). \tag{A17}$$

The coefficients $A_\alpha, a_\alpha, A_\gamma, a_\gamma, A_\sigma$, and a_σ are functions of s:

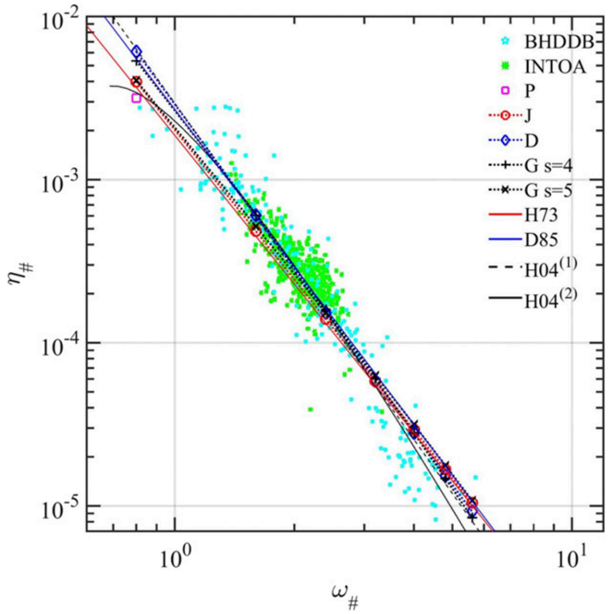

FIG. A2. Wind-wave growth function $\eta_\#(\omega_\#)$, showing field data and several published formulas as well as computations of P, J, D, and G models; see the text in Appendix for further details.

$$
\begin{aligned}
A_\alpha &= 1.30\times10^{-3}s + 1.64\times10^{-3},\\
a_\alpha &= 4.83\times10^{-1}s - 1.49,\\
A_\gamma &= 4.42\times10^{-1}s + 3.93\times10^{-1},\\
a_\gamma &= -3.63s + 19.74,\\
A_\sigma &= -5.39\times10^{-2}s + 3.44\times10^{-1}, \quad \text{and}\\
a_\sigma &= 2.05\times10^{-9}s + 5.5\times10^{-2}.
\end{aligned} \tag{A18}
$$

In the second step, the wind-wave growth function $\eta_\#(\omega_\#)$ is used to refine the parameters to expand the application range in $\omega_\#$. The analysis leads to

$$
\begin{aligned}
\alpha_G &= \alpha_1[1 - 0.3\tanh(0.1\,\omega_\#)], \quad \text{and}\\
\gamma_G &= \gamma_1[1 - 0.5\tanh(0.1\,\omega_\#)].
\end{aligned} \tag{A19}
$$

The spectral parameter σ_G was left in the same form as defined in (A17) and (A18) due to its large data scatter in the available data sources, that is, $\sigma_G = \sigma_1$.

Figure A1 shows a comparison of the spectral parameters α, γ, and σ for $s = 4$ and 5 with solid and dashed curves, respectively. The red curves represent the J model ($s = 5$), the blue curves are for the D model ($s = 4$), and the green curves are for the G model ($s = 4$ and 5). Figures 2 and 3 in the main text show several examples comparing the J, D, and G models with hurricane reconnaissance observations.

The wind-wave growth functions are among the most versatile and robust wind-wave similarity relationships. A detailed discussion was given recently by Hwang and Walsh (2016), and it is not repeated here. Of special interest to the present investigation is the function $\eta_\#(\omega_\#)$ connecting the three most important wind and wave variables: reference surface wind speed U_{10}, significant wave height H_s, and spectral peak wave period T_p. Figure A2 shows two sets of measurements: green marker for the INTOA data and cyan marker for a combined set (labeled BHDDB) assembled from five field experiments under steady wind forcing and near-neutral stability conditions (Burling 1959; Hasselmann et al. 1973; Donelan et al. 1985; Dobson et al. 1989; Babanin and Soloviev 1998).

Also shown in the figure are several published formulas of $\eta_\#(\omega_\#)$: H73 (Hasselmann et al. 1973), D85 (Donelan et al. 1985), and H04 (Hwang and Wang 2004). Hwang and Wang (2004) obtain the first- and second-order fittings of the BHDDB dataset, and they are labeled H04$^{(1)}$ and H04$^{(2)}$ in the figure. In addition to expanding the $\omega_\#$ range in the combined database for fitting the wave growth functions, Hwang and Wang (2004) describe a mathematical connection between fetch, duration, and wave age similarities. The mathematical connection makes it feasible to use the more abundant and better quality fetch-limited experimental results to fill in gaps in the rarely occurred and difficult-to-acquire duration-limited experiments, especially for the early stage of wave development. The H04$^{(1)}$ and H04$^{(2)}$ functions for fetch, duration, and wave age similarity relationships are all derived from the BHDDB data.

For any spectral model function, given a range of U_{10} and $\omega_\#$ (and s for the Y and G models), we can produce the $\eta_\#(\omega_\#)$ relationship corresponding to the given spectral model because ω_p for calculating the spectrum can be obtained from $g\omega_\#/U_{10}$. The computed spectrum is then integrated to yield the wave variance so a range of $\eta_\#$ and $\omega_\#$ of the given spectral model can be readily obtained.

The results applied to the P, J, D, and G ($s = 4$ and 5) models are shown in Fig. A2 with connected markers. The P model is for fully developed seas, so we only compute it for $\omega_\# = 0.8$. For the other models the $\omega_\#$ range is 0.8 to 5.6 in steps of 0.8. Serving as a cross check of the computation, we highlight the close agreement between the pairs of growth function formula and model computation: red curves for the H73 formula and J model and blue curves for the D85 formula and D model. Given the large scatter in the field data, all spectral models discussed in this appendix yield very good agreement with the field measurements describing the similarity relationship connecting the three integral wind and wave parameters: U_{10}, H_s, and T_p.

REFERENCES

Babanin, A. V., and Y. P. Soloviev, 1998: Field investigation of transformation of the wind wave frequency spectrum with fetch and the stage of development. *J. Phys. Oceanogr.*, **28**, 563–576, doi:10.1175/1520-0485(1998)028<0563:FIOTOT>2.0.CO;2.

Badulin, S. I., A. N. Pushkarev, D. Resio, and V. E. Zakharov, 2005: Self-similarity of wind-driven seas. *Nonlinear Processes Geophys.*, **12**, 891–946, doi:10.5194/npg-12-891-2005.

——, A. V. Babanin, D. Resio, and V. Zakharov, 2007: Weakly turbulent laws of wind–wave growth. *J. Fluid Mech.*, **591**, 339–378, doi:10.1017/S0022112007008282.

Black, P. G., and Coauthors, 2007: Air–sea exchange in hurricanes: Synthesis of observations from the Coupled Boundary Layer Air–Sea Transfer experiment. *Bull. Amer. Meteor. Soc.*, **88**, 357–374, doi:10.1175/BAMS-88-3-357.

Burling, R. W., 1959: The spectrum of waves at short fetches. *Dtsch. Hydrogr. Z.*, **12**, 96–117, doi:10.1007/BF02019818.

Dobson, F., W. Perrie, and B. Toulany, 1989: On the deep-water fetch laws for wind-generated surface gravity waves. *Atmos.–Ocean*, **27**, 210–236, doi:10.1080/07055900.1989.9649334.

Donelan, M. A., J. Hamilton, and W. H. Hui, 1985: Directional spectra of wind-generated waves. *Philos. Trans. Roy. Soc. London*, **A315**, 509–562, doi:10.1098/rsta.1985.0054.

Dunion, J. P., and C. S. Velden, 2002: Application of surface-adjusted GOES low-level cloud-drift winds in the environment of Atlantic tropical cyclones. Part II: Integration into surface wind analysis. *Mon. Wea. Rev.*, **130**, 1347–1355, doi:10.1175/1520-0493(2002)130<1347:AOSAGL>2.0.CO;2.

——, S. H. Houston, C. S. Velden, and M. D. Powell, 2002: Application of surface-adjusted GOES low-level cloud-drift winds in the environment of Atlantic tropical cyclones. Part I: Methodology and validation. *Mon. Wea. Rev.*, **130**, 1333–1346, doi:10.1175/1520-0493(2002)130<1333:AOSAGL>2.0.CO;2.

Esquivel-Trava, B., F. J. Ocampo-Torres, and P. Osuna, 2015: Spatial structure of directional wave spectra in hurricanes. *Ocean Dyn.*, **65**, 65–76, doi:10.1007/s10236-014-0791-9.

Fan, Y., and W. E. Rogers, 2016: Drag coefficient comparisons between observed and model simulated directional wave spectra under hurricane conditions. *Ocean Modell.*, **102**, 1–13, doi:10.1016/j.ocemod.2016.04.004.

——, I. Ginis, and T. Hara, 2009a: The effect of wind–wave–current interaction on air–sea momentum fluxes and ocean response in tropical cyclones. *J. Phys. Oceanogr.*, **39**, 1019–1034, https://doi.org/10.1175/2008JPO4066.1.

——, ——, ——, C. W. Wright, and E. J. Walsh, 2009b: Numerical simulations and observations of surface wave fields under an extreme tropical cyclone. *J. Phys. Oceanogr.*, **39**, 2097–2116, doi:10.1175/2009JPO4224.1.

Gagnaire-Renou, E., M. Benoit, and S. I. Badulin, 2011: On weakly turbulent scaling of wind sea in simulations of fetch-limited growth. *J. Fluid Mech.*, **669**, 178–213, doi:10.1017/S0022112010004921.

García-Nava, H., F. J. Ocampo-Torres, P. Osuna, and M. A. Donelan, 2009: Wind stress in the presence of swell under moderate to strong wind conditions. *J. Geophys. Res.*, **114**, C12008, doi:10.1029/2009JC005389.

Grachev, A. A., C. W. Fairall, J. E. Hare, J. B. Edson, and S. D. Miller, 2003: Wind stress vector over ocean waves. *J. Phys. Oceanogr.*, **33**, 2408–2429, doi:10.1175/1520-0485(2003)033<2408:WSVOOW>2.0.CO;2.

Hasselmann, K., and Coauthors, 1973: Measurements of wind-wave growth and swell decay during the Joint North Sea Wave Project (JONSWAP). Ergänzungsheft zur Deutschen Hydrographischen Zeitschrift Reihe A(8) 12, 95 pp.

——, D. B. Ross, P. Müller, and W. Sell, 1976: A parametric wave prediction model. *J. Phys. Oceanogr.*, **6**, 200–228, doi:10.1175/1520-0485(1976)006<0200:APWPM>2.0.CO;2.

Holthuijsen, L. H., M. D. Powell, and J. D. Pietrzak, 2012: Wind and waves in extreme hurricanes. *J. Geophys. Res.*, **117**, C09003, doi:10.1029/2012JC007983.

Hwang, P. A., 2006a: Duration- and fetch-limited growth functions of wind-generated waves parameterized with three different scaling wind velocities. *J. Geophys. Res.*, **111**, C02005, https://doi.org/10.1029/2005JC003180.

——, 2006b: Doppler frequency shift in ocean wave measurements: Frequency downshift of a wavenumber component by advection of background wave orbital velocity. *J. Geophys. Res.*, **111**, C06033, https://doi.org/10.1029/2005JC003072.

——, 2016: Fetch- and duration-limited nature of surface wave growth inside tropical cyclones: With applications to air–sea exchange and remote sensing. *J. Phys. Oceanogr.*, **46**, 41–56, doi:10.1175/JPO-D-15-0173.1.

——, and O. H. Shemdin, 1988: The dependence of sea surface slope on atmospheric stability and swell conditions. *J. Geophys. Res.*, **93**, 13 903–13 912, doi:10.1029/JC093iC11p13903.

——, and D. W. Wang, 2001: Directional distributions and mean square slopes in the equilibrium and saturation ranges of the wave spectrum. *J. Phys. Oceanogr.*, **31**, 1346–1360, doi:10.1175/1520-0485(2001)031<1346:DDAMSS>2.0.CO;2.

——, and ——, 2004: Field measurements of duration limited growth of wind-generated ocean surface waves at young stage of development. *J. Phys. Oceanogr.*, **34**, 2316–2326, https://doi.org/10.1175/1520-0485(2004)034<2316:FMODGO>2.0.CO;2; Corrigendum, **35**, 268–270, https://doi.org/10.1175/JPO-2731.1.

——, and M. A. Sletten, 2008: Energy dissipation of wind-generated waves and whitecap coverage. *J. Geophys. Res.*, **113**, C02012, doi:10.1029/2007JC004277; Corrigendum, **114**, C02015, doi:10.1029/2008JC005244.

——, and E. J. Walsh, 2016: Azimuthal and radial variation of wind-generated surface waves inside tropical cyclones. *J. Phys. Oceanogr.*, **46**, 2605–2621, doi:10.1175/JPO-D-16-0051.1.

——, and Y. Fan, 2017: Effective fetch and duration of tropical cyclone wind fields estimated from simultaneous wind and wave measurements: Surface wave and air–sea exchange computation. *J. Phys. Oceanogr.*, **47**, 447–470, doi:10.1175/JPO-D-16-0180.1.

——, H. García-Nava, and F. J. Ocampo-Torres, 2011: Observations of wind wave development in mixed seas and unsteady wind forcing. *J. Phys. Oceanogr.*, **41**, 2343–2362, doi:10.1175/JPO-D-11-044.1.

——, D. M. Burrage, D. W. Wang, and J. C. Wesson, 2013: Ocean surface roughness spectrum in high wind condition for microwave backscatter and emission computations. *J. Atmos. Oceanic Technol.*, **30**, 2168–2188, doi:10.1175/JTECH-D-12-00239.1.

——, X. Li, and B. Zhang, 2017: Retrieving hurricane wind speed from dominant wave parameters. *IEEE J. Sel. Top. Appl. Earth Obs. Remote Sens.*, **10**, 2589–2598, doi:10.1109/JSTARS.2017.2650410.

Janssen, P., 2004: *The Interaction of Ocean Waves and Wind.* Cambridge University Press, 300 pp.

Kahma, K. K., and C. J. Calkoen, 1992: Reconciling discrepancies in the observed growth of wind-generated waves. *J. Phys. Oceanogr.*, **22**, 1389–1405, doi:10.1175/1520-0485(1992)022<1389:RDITOG>2.0.CO;2.

——, and ——, 1994: Growth curve observations. *Dynamics and Modeling of Ocean Waves*, G. J. Komen et al., Eds., Cambridge University Press, 74–182.

Kitaigorodskii, S. A., 1961: Application of the theory of similarity to the analysis of wind generated wave motion as a stochastic process. *Izv. Akad. Nauk SSSR Ser. Geofiz.*, **1**, 105–117.

Komen, G. J., L. Cavaleri, M. Donelan, K. Hasselmann, S. Hasselmann, and P. A. E. M. Jessen, Eds., 1994: *Dynamics and Modeling of Ocean Waves*. Cambridge University Press, 532 pp.

Moon, I.-J., I. Ginis, T. Hara, H. L. Tolman, C. W. Wright, and E. J. Walsh, 2003: Numerical simulation of sea surface directional wave spectra under hurricane wind forcing. *J. Phys. Oceanogr.*, **33**, 1680–1706, doi:10.1175/2410.1.

Ocampo-Torres, F. J., H. García-Nava, R. Duranzo, P. Osuna, G. M. Díaz Méndez, and H. C. Graber, 2011: The INTOA Experiment: A study of ocean-atmosphere interactions under moderated to strong offshore winds and opposing swell conditions in the Gulf of Tehuantepec, Mexico. *Bound.-Layer Meteor.*, **138**, 433–451, doi:10.1007/s10546-010-9561-5.

Phillips, O. M., 1958a: The equilibrium range in the spectrum of wind-generated waves. *J. Fluid Mech.*, **4**, 426–434, doi:10.1017/S0022112058000550.

——, 1958b: On some properties of the spectrum of wind-generated ocean waves. *J. Mar. Res.*, **16**, 231–240.

——, 1985: Spectral and statistical properties of the equilibrium range in wind-generated gravity waves. *J. Fluid Mech.*, **156**, 505–531, doi:10.1017/S0022112085002221.

Pierson, W. J., 1964: The interpretation of wave spectrums in terms of the wind profile instead of the wind measured at a constant height. *J. Geophys. Res.*, **69**, 5191–5203, doi:10.1029/JZ069i024p05191.

——, and L. Moskowitz, 1964: A proposed spectral form for fully developed wind seas based on the similarity theory of S. A. Kitaigorodskii. *J. Geophys. Res.*, **69**, 5181–5190, doi:10.1029/JZ069i024p05181.

Powell, M. D., and S. H. Houston, 1998: Surface wind fields of 1995 Hurricanes Erin, Opal, Luis, Marilyn, and Roxanne at landfall. *Mon. Wea. Rev.*, **126**, 1259–1273, doi:10.1175/1520-0493(1998)126<1259:SWFOHE>2.0.CO;2.

——, ——, and T. A. Reinhold, 1996: Hurricane Andrew's landfall in south Florida. Part I: Standardizing measurements for documentation of surface wind fields. *Wea. Forecasting*, **11**, 304–328, doi:10.1175/1520-0434(1996)011<0304:HALISF>2.0.CO;2.

Price, J. F., 1981: Upper ocean response to a hurricane. *J. Phys. Oceanogr.*, **11**, 153–175, doi:10.1175/1520-0485(1981)011<0153:UORTAH>2.0.CO;2.

Sverdrup, H. U., and W. H. Munk, 1947: Wind, sea, and swell: Theory of relations for forecasting. U.S. Navy Hydrographic Office Tech. Rep. 1, 56 pp.

Walsh, E. J., D. W. Hancock, D. E. Hines, R. N. Swift, and J. F. Scott, 1985: Directional wave spectra measured with the surface contour radar. *J. Phys. Oceanogr.*, **15**, 566–592, doi:10.1175/1520-0485(1985)015<0566:DWSMWT>2.0.CO;2.

——, ——, ——, ——, and ——, 1989: An observation of the directional wave spectrum evolution from shoreline to fully developed. *J. Phys. Oceanogr.*, **19**, 670–690, doi:10.1175/1520-0485(1989)019<0670:AOOTDW>2.0.CO;2.

——, and Coauthors, 2002: Hurricane directional wave spectrum spatial variation at landfall. *J. Phys. Oceanogr.*, **32**, 1667–1684, doi:10.1175/1520-0485(2002)032<1667:HDWSSV>2.0.CO;2.

Wright, C. W., and Coauthors, 2001: Hurricane directional wave spectrum spatial variation in the open ocean. *J. Phys. Oceanogr.*, **31**, 2472–2488, doi:10.1175/1520-0485(2001)031<2472:HDWSSV>2.0.CO;2.

Young, I. R., 1988: Parametric hurricane wave prediction model. *J. Waterw. Port Coastal Ocean Eng.*, **114**, 637–652, doi:10.1061/(ASCE)0733-950X(1988)114:5(637).

——, 1998: Observations of the spectra of hurricane generated waves. *Ocean Eng.*, **25**, 261–276, doi:10.1016/S0029-8018(97)00011-5.

——, 1999: *Wind Generated Ocean Waves.* Elsevier, 288 pp.

——, 2006: Directional spectra of hurricane wind waves. *J. Geophys. Res.*, **111**, C08020, https://doi.org/10.1029/2006JC003540.

——, and G. Ph. van Vledder, 1993: A review of the central role of nonlinear interactions in wind-wave evolution. *Philos. Trans. Roy. Soc. London*, **A342**, 505–524, doi:10.1098/rsta.1993.0030.

Zakharov, V. E., 2005: Theoretical interpretation of fetch limited wind-driven sea observations. *Nonlinear Processes Geophys.*, **12**, 1011–1020, doi:10.5194/npg-12-1011-2005.

——, S. I. Badulin, P. A. Hwang, and G. Caulliez, 2015: Universality of sea wave growth and its physical roots. *J. Fluid Mech.*, **780**, 503–535, doi:10.1017/jfm.2015.468.

Zhang, G., X. Li, W. Perrie, P. Hwang, B. Zhang, and X. Yang, 2017: A hurricane wind speed retrieval model for C-band RADARSAT-2 cross-polarization ScanSAR images. *IEEE Trans. Geosci. Remote Sens.*, **55**, 4766–4774, https://doi.org/10.1109/TGRS.2017.2699622.

Zhang, J. A., and E. W. Uhlhorn, 2012: Hurricane sea surface inflow angle and an observation-based parametric model. *Mon. Wea. Rev.*, **140**, 3587–3605, doi:10.1175/MWR-D-11-00339.1.